Energy Conversion and Management 349 (2026) 120838

Contents lists available at ScienceDirect

Energy Conversion and Management

journal homepage: www.elsevier.com/locate/enconman

Design and optimisation of a novel solar-driven ORC-based polygeneration system with hybrid PVT, cascade refrigeration, and PEM electrolysis

Jesús García-Domínguez [a,*], J. Daniel Marcos [a], Ana M. Blanco-Marigorta [b], Pablo A. García-Salaberri [c,d]

[a] Universidad Nacional de Educación a Distancia, UNED, E.T.S. Ingenieros Industriales, Departamento de Ingeniería Energética, C/ Juan del Rosal 12, Madrid 28040, Spain
[b] Universidad de Las Palmas de Gran Canaria, Departamento de Ingeniería de Procesos, Edificio de Ingenierías-Tafira Baja, Las Palmas, G.C. 35017, Spain
[c] Universidad Rey Juan Carlos de Madrid, Department of Chemical and Environmental Technology (ESCET), Universidad Rey Juan Carlos, C/ Tulipán s/n, Móstoles, Madrid 28933, Spain
[d] Instituto de Investigación de Tecnologías para la Sostenibilidad, Universidad Rey Juan Carlos, C/Tulipán s/n Móstoles, Madrid 28933, Spain

ARTICLE INFO

Keywords:
Polygeneration
Organic rankine cycle
Photovoltaic–thermal (PVT) concentrating collectors
Cascaded refrigeration system
PEM electrolyser

ABSTRACT

This study presents the design, modelling, and optimisation of a novel zero-emissions polygeneration system fully powered by renewable energy sources. A new integration approach supported by an advanced optimisation framework is proposed to enhance the thermodynamic performance and overall efficiency. The system uniquely combines a hybrid Photovoltaic-Thermal (PVT) powered Organic Rankine Cycle (ORC) employing flexible Perovskite Solar Cell (PSC) technology, a double-effect compression-absorption refrigeration subsystem, and hydrogen production via a Proton Exchange Membrane (PEM) electrolyser. The cascading configuration maximises energy utilisation by recovering low-grade thermal energy, promoting synergistic operation, enabling simultaneous multi-carrier generation, and reducing exergy losses compared to standalone systems. Its applications are particularly relevant for both buildings and energy-intensive industrial processes, where integrated renewable solutions can provide high efficiency, flexibility, and emission-free operation. An advanced hybrid optimisation methodology coupling an Artificial Neural Network (ANN) with a multi-objective genetic algorithm is applied to identify optimal configurations through performance-cost trade-offs. For a three-objective function, the optimum design achieves an exergy efficiency of 19.1 %, net power output of 69.6 kW, and a cost rate of $ 14.2/h. Over a 20-year operation period, the system shows strong economic viability, yielding a payback period of 5.7 years, a Net Present Value (NPV) of $602,000, and an Internal Rate of Return (IRR) of 11.6 %.

1. Introduction

Solar concentrator-based polygeneration systems, coupled with Organic Rankine Cycle (ORC) technology, represent a promising avenue for sustainable on-site energy production for industries and buildings. These systems are designed to maximise energy efficiency and resource utilisation for the simultaneous production of multiple forms of energy, such as electricity, heating, cooling, and hydrogen.

ORC systems are considered as one of the most typical technologies used as prime mover for power generation in distributed and polygeneration energy systems [1]. This technology is particularly suitable due to its flexibility and scalability by using low-to medium-temperature heat sources like solar thermal, geothermal energy, and industrial waste heat [2]. Several different cycle arrangements can be used in ORC systems, each tailored to specific applications and operating conditions. The heat source temperature and the evaporation pressure are key parameters for the suitability of the ORC configuration and the corresponding cycle performance [3]. For heat source temperatures lower than 240 °C, a dual-pressure evaporation ORC is unfitting, being the single-pressure regenerative recuperated superheated ORC the most efficient arrangement [4]. Javed and Tiwari [5] compared basic, recuperative, and regenerative ORC configurations with different organic working fluids from the energy and economic viewpoints. They highlighted that the regenerative ORC shows an enhancement of 36.6 % and 25.2 % compared to basic and recuperative cycles. The selection of the organic fluid is another key factor for solar ORC systems. Isentropic fluids the most suitable for subcritical ORC applications due to the vapor

* Corresponding author at: International Doctoral School of UNED, Industrial Technologies, Spain.
E-mail address: jgarcia5088@alumno.uned.es (J. García-Domínguez).

https://doi.org/10.1016/j.enconman.2025.120838
Received 10 July 2025; Received in revised form 23 November 2025; Accepted 26 November 2025
Available online 13 December 2025

Nomenclature

A	Area, m^2
D	diameter, mm
ΔT	temperature difference, °C
E	activation energy, kJ/mol
$\dot{Ex}$	exergy, kW
$\dot{ex}$	specific exergy, kJ/kg
F	Faraday constant, 96485 C/mol
h	enthalpy, kJ/K
ht	heat transfer coefficient, kW/(m^2 K)
I_b	direct solar irradiance, kW/m^2
J	current density, A/cm^2
k	thermal conductivity, kW/(m K)
L	length of PTC, m
$\dot{m}$	mass flow rate, kg/s
n	system's lifespan
N_c	number of solar collectors
n_c	number of cells
$\dot{n}$	molar flow rate, mol/s
P	pressure, kPa
$\dot{Q}$	thermal power, kW
$\dot{q}$	heat rate per PTC unit length, kW/m
R	universal gas constant, 8.314 J/(mol K)
r	discount rate
s	entropy, kJ/kg K
T	temperature, °C
t	annual operating hours
U	overall heat transfer coefficient, kW/(m^2 K)
V	voltage, V
$\dot{W}$	electric power, kW
w_{ap}	aperture width of PTC, m
X	mass fraction
Y	exergy destruction ratio
Y^*	irreversibility ratio

Greek symbols

α	absorptance
α_a	transfer coefficient of the anode
α_c	transfer coefficient of the cathode
δ	thickness
ε	emissivity
η	efficiency
η_F	Faraday's efficiency
θ	solar incidence angle on the PTC
λ	water content
μ	chemical potential, kJ/kg
σ	Stefane Boltzmann constant, kW/(m^2K^4)
σ_{PEM}	ionic conductivity, S/cm
τ	transmittance
φ	maintenance cost coefficient

Subscripts

0	dead conditions
a	anode
amb	ambient
abs	absorber
bio	biomass input
bh	biomass heater
c	cathode
cas	cascade refrigeration system
ch	chemical
cnd	heat conduction
cnv	heat convection
co	compressor
cool	cooling capacity
cond	condenser
cov	glass cover
D	destruction
e	exterior
el	electricity
en	energy
eva	evaporator
ex	exergy
F	fuel
hc-ld	high condenser – low desorber
hd	hight desorber
heat	heating capacity
i	interior
in	inlet
j	state
k	component
L	loss
ls	live steam
m	membrane
th	thermal
ohm	ohmic
opt	optical
OT	overlap temperature
out	outlet
P	product
ph	physical
poly	polygeneration
rad	heat radiation
rec	recuperator
res	renewable energy sources
s	isentropic
SH	superheating
sol	solar absorption
st	storage tank
S,pump	solution pumps
tot	total
tub	absorber tube
u	useful absorbed energy
z	subsystem

leaving the turbine after the expansion remains saturated with no condensation, and due to small-medium vaporizing enthalpies [6–8].

The utilisation of low- to medium-temperature solar energy as the primary energy source for the ORC offers a dependable and sustainable solution [9]. Loni et al. [10] conducted an extensive review of different solar collector configurations —both non-concentrating and concentrating—and conclude that solar Parabolic Trough Collectors (PTCs) are among the most efficient technologies, achieving overall system efficiencies exceeding 20 %. Generally, solar thermal collectors present high exergy destruction rates. Nevertheless, hybrid Photovoltaic Thermal (PVT) collectors for dual production of thermal and electrical energies could help maximise the energy yield compared stand-alone thermal collectors [11]. A detailed classification of PVT systems is presented by Herez et al. [12] considering types of PV cell and solar thermal collector, working fluid, glazing, and thermal absorber. As for concentrating solar technologies, recent studies have shown that hybrid PTC-

PV can get overall thermal and electrical efficiencies of 70 % and 25 %, respectively [13,14]. In literature, different design arrangements and optical systems are proposed applicable for PTC-PV. For thermally coupled collectors—where the thermal subsystem's operating temperature is constrained by the PV cells' thermal limits—Ju et al. [15] conducted a detailed review focusing on heat extraction methods to enhance overall system efficiency while maintaining photovoltaic performance. The geometry of the receiver is a key feature of the collector. Mortadi and El Fadar [16] analysed and compared a semi-cylindrical receiver with the main three typical receivers of PTC-PV, that is rectangular, tubular and triangular. The results proved that semi-cylindrical receiver achieved the highest thermal efficiency with 0.77, followed by the tubular receiver with 0.63, then the triangular receiver with a value of 0.61, and finally the rectangular receiver with 0.56. A PVT module is commonly constructed by integrating a PV layer onto a thermal absorber, typically using mechanical fastening or chemical adhesive bonding methods to ensure effective thermal and structural coupling [17]. From a thermal perspective, minimising the gap between the two layers is crucial to enhance heat transfer from the PV cell to the thermal absorber, thereby improving the overall efficiency of the module. From a mechanical viewpoint, selecting the appropriate materials is essential to ensure a durable joint and prevent PV cell cracking caused by the different thermal expansion of both components.

Unlike traditional silicon-based solar cells, which are inflexible and challenging to install, thin-film PV cells offer high efficiency combined with adaptability due to their flexible substrates. They are typically made from various semiconductor materials, such as cadmium telluride (CdTe), amorphous silicon (a-Si), and copper indium gallium selenide (CIGS), offering lower manufacturing costs and the flexibility to be integrated into a wider range of applications [18]. One of the emerging PV cell technologies are the Perovskite Solar Cells (PSC). These are typically made from organic-inorganic hybrid compounds using low-cost materials and innovative manufacturing techniques, such as roll-to-roll processing, which includes spin coating, printing, or spray coating [19,20]. Recent research has shown that approximately in the last 12 years, the Power Conversion Efficiency (PCE) of PSC has increased from just 9.7 % [21] to over 30 % [22]. Despite the highest achievable PCE of all-perovskite tandem solar cells is about 46 % [23], at the laboratory scale [24], certified PCEs have reached 30.1 % for all-perovskite tandem solar cells and 34.6 % for perovskite/silicon tandem configurations. A key challenge in PVT technologies is integrating PSC with solar-thermal absorbers to simultaneously generate electricity and heat. Huang et al. [25] recently developed a prototype achieving efficient solar spectrum utilisation, maintaining optimal PV temperatures, and producing both low- and high-temperature heat, with an overall exergy efficiency of approximately 30 %. Although the integration of perovskite photovoltaic technology within hybrid PVT collectors enables high theoretical electrical efficiency and compact design, the long-term stability of perovskite materials under real operating conditions remains a major challenge for large-scale deployment. Perovskite layers are sensitive to environmental factors such as moisture, oxygen, UV radiation, and temperature fluctuations, which can significantly degrade their performance over time. Recent advances in encapsulation, compositional engineering, and tandem structures have improved operational stability [26,27].

Producing green hydrogen by water electrolysis through bottoming cycle integrated into solar-driven polygeneration systems represents a novel approach to maximise overall system efficiency [28,29]. Hydrogen is mainly produced by electrolysis, splitting water into oxygen and hydrogen. Three major water electrolysis techniques are known [30]: alkaline conditions (AEL), acidic conditions via Proton Exchange Membrane (PEM), and steam electrolysis through Solid Oxide Electrolysis Cells (SOEC). Unlike SOEC that require high operating temperatures ranging 700–1000 °C, AEL and PEM electrolysers are more suitable to be utilised in low-medium temperature solar-based polygeneration applications, which typically operate below 100 °C [31]. Due to its commercial availability, efficiency, adaptability and fast responsiveness related to Power-to-X approach, PEM water electrolysers are considered the most promising technology for hydrogen production [32–35]. Few studies have been found in the literature integrating PEM electrolysers together with solar ORC-based Combined Cooling, Heating and Power (CCHP). Karabuga et al. [36] conducted an experimental study integrating an ORC for power generation, driven by an evacuated tube heat pipe solar collector, with a PEM electrolyser for hydrogen production. The system achieved a maximum exergy efficiency of 9.56 % and a hydrogen production cost of $ 0.98/kg. Shabani and Babaelahi [37] proposed and evaluated an innovative solar-based polygeneration system integrated with solar PTCs, multi-effect distillation, PEM electrolyser, Kalina cycle, ORC, Brayton cycle, and ejector cooling for the simultaneous production of electricity, fresh water, hydrogen, and cooling energy. The results showed that the yielded net power output is 32.3 MW, and the ejector Coefficient of Performance (COP) is 0.32; while that overall energy and exergy efficiencies were 38.4 % and 35.6 %, respectively. Fouda et al. [38] evaluated a large-scale solar ORC-based cogeneration system for simultaneous production of hydrogen and cooling, through a PEM electrolyser and a double-effect absorption refrigeration cycle. The overall energy and exergy efficiencies found for R141b as working fluid when Direct Normal Irradiance (DNI) was set at 950 W/m^2 are about 17 % and 14 %, respectively. A new solar powered multigeneration system for power, cooling, and hydrogen production was analysed and optimised by Qing [39]. This approach is formed by SPTCs integrated with thermal energy storage, a dual-pressure ORC, a vapor compression refrigeration cycle, a PEM electrolyser and a Claude hydrogen liquefaction unit. The results indicated that the system generated 13.4 MW of power, 3.4 MW of cooling, and 27.3 kg/h of liquified hydrogen, yielding an exergy efficiency of 9.03 % and a payback period of 6.04 years. A solar power-based combined multigeneration plant was evaluated by Yuksel et al. [40] including steam Rankine cycle, ORC, PEM electrolyser, single-effect absorption heat-pump, as well as freshwater production and ammonia, methane and urea production units. The total energy and exergy efficiencies achieved were 66.1 % and 61.6 %, respectively. A solar hybrid based polygeneration system was proposed by Raja and Huang [41] consisting of solar PTCs, PVT collectors, ORC, single-effect absorption heat pump and vapor compression heat-pump, and two electrolysers for hydrogen production. At a solar fluid outlet temperature of 477 K, the system achieved overall energy and exergy efficiencies of 12.0 % and 54.7 %, respectively.

Most of the multigeneration systems that integrate refrigeration cycles are focused on air conditioning applications to produce chilled water, typically ranging 7–12 °C. However, many industrial applications require low-temperature cooling ranging from food conservation and ice production to quick freezing medical items and pharmaceutical products preservation. Low-temperature refrigeration systems are primarily driven by Vapor Compression Refrigeration Cycles (VCRC), which rely on electricity often derived from fossil fuels, leading to significant environmental concerns. New system layouts, like multistage compression systems, intercooling, and cascade approaches combining a VCRC with a vapor absorption refrigeration cycle (VARC), are promising alternatives in view to increase system performance [42]. Past and recent investigations have shown that hybrid cooling systems consisting of cascaded vapor absorption-compression refrigeration cycles can lead to a substantial reduction in energy consumption. Most of the investigations have been focused on stand-alone single stage absorption-vapor compression cascade refrigeration cycles. Various refrigerants are used in compression cycles (such as R22, R134a, R717, and R410A), while absorption cycles utilise different fluid mixtures (for example, H_2O/LiBr and NH_3/H_2O). [43–51]. However, very limited literature is available on double-stage absorption-vapor compression cascade approaches integrated with solar-driven polygeneration systems. Colorado and Rivera [52] analysed, for the first time in the literature, a compression-absorption series flow double-stage refrigeration system.

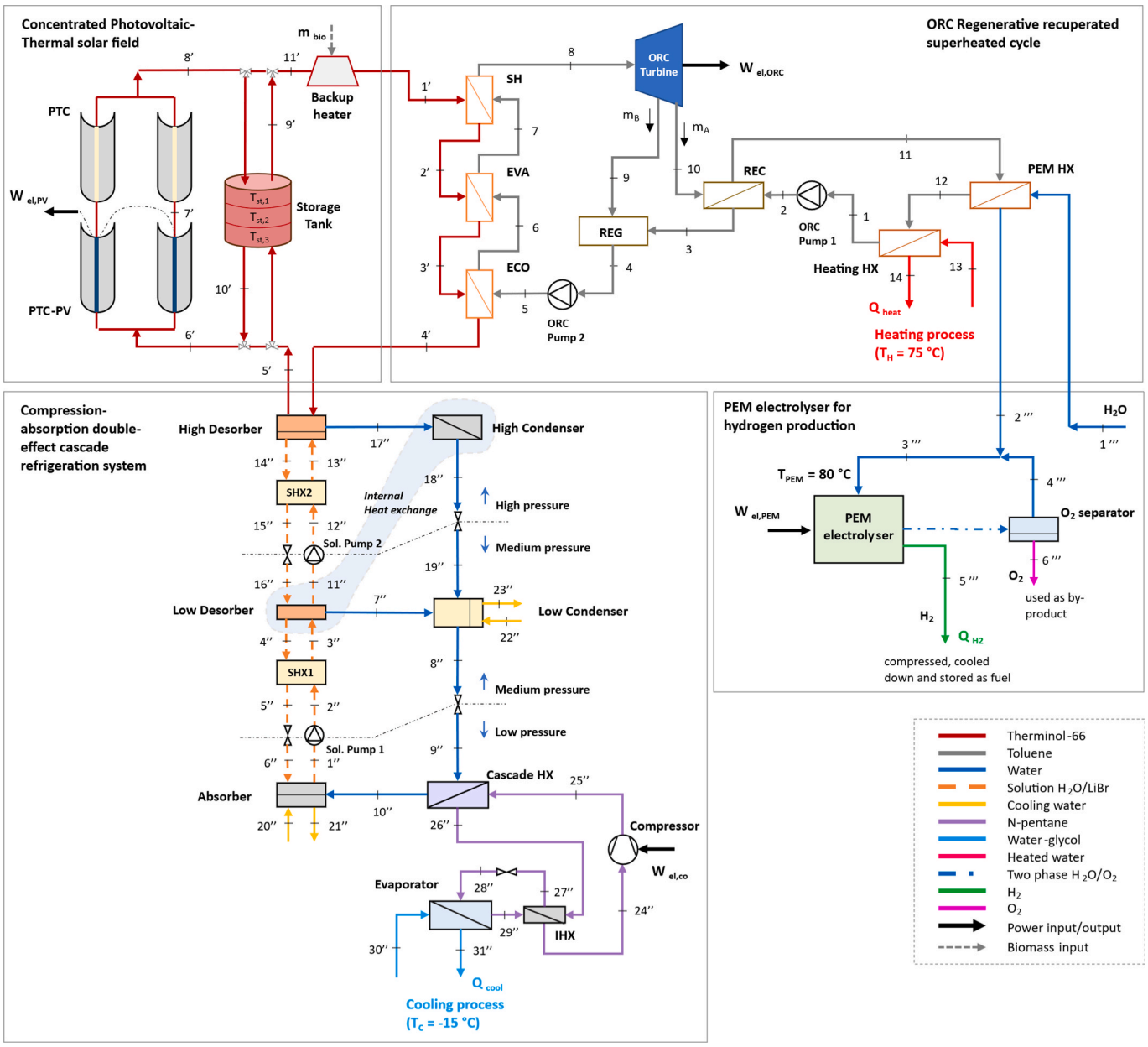

Fig. 1. Schematic of the polygeneration system.

They conducted a comparison with a conventional vapor compression cooling scheme, and a compression-absorption single-stage system from the First and Second Law. The compression cycle employed CO_2 and R134a as refrigerants, whereas the absorption cycle utilised a water/lithium bromide working pair. The authors concluded that the power consumption in the cascaded systems was 45 % lower than in conventional vapor compression cycle. In terms of COP, operating with R134a-H_2O/LiBr and for an evaporator temperature of 263 K, the compression-absorption double-stage system obtained a value of 0.91, while the single-stage system achieved 0.58. Regarding the desorber temperature, they concluded that the compression-absorption single-stage system requires a temperature ranging between 340 K and 355 K, while the double-stage system temperatures varied between 380 K and 420 K. Dixit et al. [53] proposed a novel cascade refrigeration scheme combining a two-stage absorption refrigeration cycle with a compression refrigeration cycle arranged both in series and in parallel. The results demonstrated an 89.3 % reduction in electricity consumption compared to a standalone vapor compression system. For evaporator temperatures of 1 °C (compression) and 6 °C (absorption), and a desorber temperature of 65 °C, the system achieved an overall COP of 0.38 and an exergetic efficiency of 12.98 %. Cimsit [54] investigated a double-effect absorption–vapor compression cascade system using R-134a in the vapor compression section and H_2O/LiBr in the absorption section. The study compared the energy and exergy performances of this configuration with those of a single-effect cascade system and a conventional vapor compression cycle. At an evaporator temperature of 275 K and a desorber temperature of 408 K, the double-stage system achieved a COP of 1.12, outperforming the single-stage system, which had a COP of 0.71. In terms of exergy efficiency, a value of 15.48 % can be achieved with the former, while 13.97 % with the latter. A series flow double-effect cascaded absorption-vapor compression system was analysed and optimised by Mussati et al. [55] in terms of best configuration, sizing of heat transfer areas and operating conditions. The obtained optimal total heat transfer area is about 7.3 % smaller than reported by Colorado and Rivera [52]. There is no study in the literature related to solar-driven polygeneration systems using bottoming double-stage

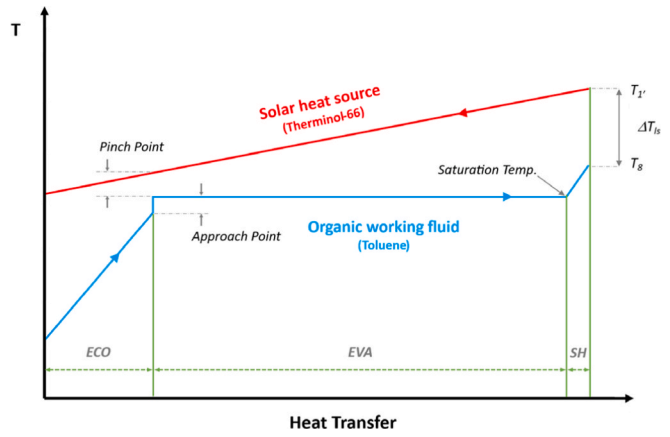

Fig. 2. Temperature-Heat transfer diagram in the ORC evaporator.

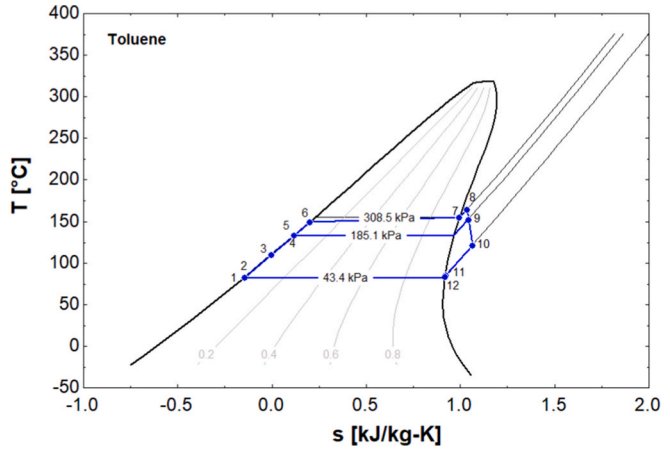

Fig. 3. T-s diagram of the regenerative recuperated superheated ORC.

absorption-compression cascade cycles for low-temperature cooling.

In the design of thermodynamic systems, a common strategy involves selecting critical input variables to optimise overall system performance. Multi-Objective Optimisation (MOO) methods are essential where multiple conflicting goals must be addressed simultaneously. Often it is sought to maximise system efficiency while minimising economic cost. MOO assists in identifying trade-offs by providing decision-makers with a set of optimal solutions, allowing them to select based on their specific preferences or constraints. Recent advancements in energy systems optimisation have increasingly leveraged Artificial Neural Networks (ANNs) to enhance the performance of CCHP systems. These data-driven approaches have proven effective in managing the complex, nonlinear dynamics inherent in energy operations [56–59]. ANN function by mimicking the architecture of the human brain, consisting of interconnected layers of artificial neurons. Each neuron takes in input data, applies an activation function to process it, and passes the resulting output to the subsequent layer. ANNs are trained by iteratively adjusting the weights of interconnections in order to minimise prediction error, typically utilising large datasets. Once trained, ANNs can generalise from past patterns to accurately predict future system behaviour under varying conditions.

Existing ORC-based polygeneration studies rarely integrate hybrid concentrating PVT collectors with hydrogen production, and none incorporate a double-stage absorption–vapor compression cascade cycle for low-temperature cooling. Prior work often omits consistent dead-state definitions, chemical exergy, and component-level exergy analysis, while optimisation approaches are typically single-objective.

To fill these gaps, this study proposes a novel zero-emission solar-driven ORC polygeneration system producing electricity, cooling, heating, and hydrogen. This paper serves as a logical extension of the authors' recently published work [60]. It combines hybrid PVT collectors, a double-stage absorption–vapor compression cascade, and a PEM electrolyser, evaluated via First- and Second-law thermodynamic analysis. A hybrid ANN–multi-objective genetic algorithm optimisation improves multi-objective performance. The configuration maximises renewable utilisation, enhances exergy recovery, and addresses key gaps in integrated industrial polygeneration research.

In summary, the main innovations of this study can be outlined as follows:

a) The development of a novel solar-driven ORC-based polygeneration system capable of producing electricity, cooling, heating, and hydrogen with zero direct emissions.
b) The use of hybrid concentrating PVT collectors as the main renewable energy source, maximising simultaneous heat and electricity generation.
c) The implementation of a bottoming parallel-flow double-stage absorption–vapor compression cascade cycle, enabling low-temperature cooling suitable for industrial applications.
d) The establishment of a rigorous and consistent exergetic framework, addressing inconsistencies in dead-state definition and component-level exergy accounting reported in the literature.
e) The application of an advanced hybrid optimisation approach (ANN + multi-objective genetic algorithm) that outperforms conventional parametric methods by achieving multi-objective performance improvement across thermodynamic and economic indicators.

2. System description

As shown in Fig. 1, the polygeneration system evaluated in this study primarily consists of an ORC for power generation, driven by a hybrid solar system formed by PTC and PTC-PV. A double effect absorption-vapor compression cascade refrigeration system is integrated as a bottoming cycle to provide low-temperature cooling. Part of the power generated by the ORC turbine and the PTC-PV is utilised to power the PEM electrolyser for hydrogen generation. A biomass backup heater is included in the system design to provide the required thermal input during periods when the solar subsystem alone cannot meet the energy demand.

The proposed polygeneration system is inherently complex, and failures in any subsystem can affect overall performance. Nevertheless, real-time monitoring and predictive or adaptive control, along with redundancy in critical components such as backup pumps or heat exchangers, are essential to maintain reliable operation. These strategies, however, are beyond the scope of the present study, which focuses on the thermodynamic performance of the integrated system.

2.1. Organic rankine cycle

A regenerative recuperated superheated ORC is selected as the prime mover of the polygeneration system. Three different stages can be found in the single-pressure evaporator. The temperature–heat transfer diagram and the temperature–entropy (T–s) diagram for the complete evaporator are illustrated in Figs. 2 and 3, respectively. These diagrams provide insights into the heat exchange process and thermodynamic behaviour of the working fluid across the entire evaporator. Several studies are found on the literature focused on the fluid selection and the related performance analysis of ORC power systems. Dry and isentropic organic working fluids are more appropriate for ORC systems to avoid damages in the expander's blade caused by the wet vapor [61]. According to Song et al. [62], at a given heat source temperature, working fluids with higher critical temperatures and lower dryness fractions are generally more favourable due to their improved thermodynamic performance. Considering the operating temperature range of the proposed

Table 1
Input data for ORC model [66,67].

Parameter	Value
ORC evaporator inlet temperature ($T_{1'}$)	190 °C
Turbine isentropic efficiency ($\eta_{s,ORC}$)	85 %
ORC pump isentropic efficiency ($\eta_{s,ORCpump}$)	70 %
Recuperator efficiency (η_{rec})	70 %
Superheating (ΔT_{SH})	10 °C
Live steam outlet temperature ($T_8 = T_{1'} - \Delta T_{ls}$)	$T_{1\tilde{A}}$- 25
Pinch Point (*PP*)	8 K
Approach Point (*AP*)	5 K
Heating process temperature (T_{14})	75 °C

system and different literature reviews [60,63–65], toluene is chosen as the working fluid. Table A1 compares its thermophysical and environmental characteristics with other commonly proposed fluids for medium- to high-temperature ORC applications. The design parameters employed in the ORC model are summarised in Table 1.

2.2. Heat source

One of the key innovations of this study is the use of hybrid solar concentrating PVT collectors as the primary heat source for the polygeneration system. The configuration features a PTC-PV collector arranged in series with a conventional PTC, enabling simultaneous electrical and thermal energy harvesting from concentrated solar radiation. Since the electrical efficiency of PV cells decreases with increasing working temperature [70,71], the system is designed to limit excessive heating of the PV layer. To achieve this, the PTC-PV section is limited to one-third of the total collector length, while the remaining portion comprises a standard PTC, maintaining hydraulic continuity and enabling operation at medium–high temperatures (180–240 °C) without compromising PV performance.

The proposed configuration features a tubular receiver consisting of a glass cover, an air gap, a thermal absorber, and a fluid channel. The design of the PTC-PV follows a concept similar to those presented by Yan et al. [72] and Mortadi and El Fadar [16], utilising a tubular geometry. In this study, a Perovskite-based PV film is integrated directly onto the thermal absorber surface, allowing for concurrent thermal and electrical energy generation. The collectorś schematics and the diagrams of the thermal resistances are presented in Figs. 4 and 5.

The energy balance in a section of the absorber tube primarily depends on the solar energy absorbed by the collector's components and the corresponding thermal losses. In the PTC-PV, solar radiation is absorbed by the PV cell, the thermal absorber, and the glass cover, whereas in the standard PTC, only the absorber and the glass cover contribute to energy absorption. In both configurations, thermal losses occur via radiative exchange between the glass cover and the sky, and convective heat transfer from the glass cover to the ambient air. Heat losses through support brackets are assumed negligible. Additionally, due to the vacuum insulation between the absorber and the glass cover, convective heat transfer in this region is also negligible.

For the PTC-PV configuration, attaching the PSC to the thermal absorber necessitates the use of a flexible substrate. The choice of substrate is critical for ensuring high device performance, as it must combine flexibility with low sheet resistance, thermal stability, high transparency, and corrosion resistance [73,74]. Substrates are generally classified into polymer-based and metal-based types. Common flexible polymer substrates like PEN and PET are widely used but have a significant limitation—their low glass transition temperatures ($T_g < 150$ °C) [74–76], which restrict their suitability for high-temperature applications like the proposed system.

Flexible willow glass emerges as a highly promising alternative due to its ability to withstand temperatures up to 500 °C while maintaining excellent optical transparency, mechanical robustness, and compatibility with roll-to-roll fabrication processes. These characteristics make it highly suitable for integration with curved surfaces like tubular receivers, positioning it as an excellent candidate for high-efficiency flexible PSCs [74,76–78]. In terms of commercial feasibility, willow glass is available in both sheet and roll formats from multiple manufacturers (100–200 μm thickness, widths up to ~ 1.3 m, roll lengths up to ~ 300 m) [79], making it a practical option for prototype and pilot-scale perovskite modules. Recent commercial and patent activity confirms ongoing efforts to develop roll-to-roll perovskite fabrication on flexible Corning® Willow® Glass. EMC reported significant roll-to-roll printing milestones [80], and patent filings from 2023 to 2025 show continued process development [81,82]. In addition to the substrate, the efficiency of the solar cell is strongly influenced by the device's architecture. Multijunction (tandem) photovoltaic configurations provide a pathway to significantly higher PCE compared to single-junction cells by utilising multiple light-absorbing layers with complementary bandgaps [83,84]. For this study, a flexible all-perovskite tandem solar cell with a reported PCE of 24.7 % is adopted as the performance reference [85].

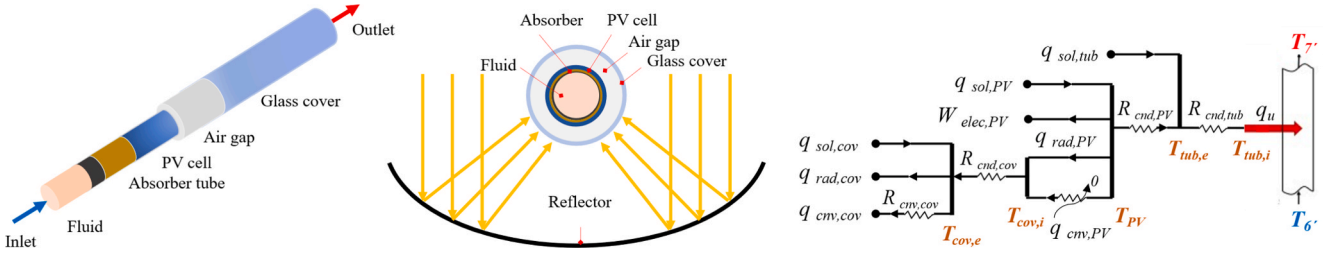

Fig. 4. Hybrid Parabolic Trough Collector-Photovoltaic (PTC-PV).

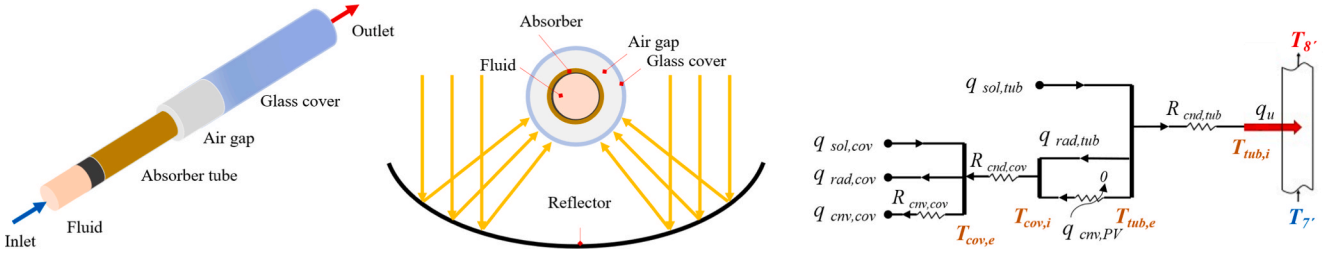

Fig. 5. Parabolic Trough Collector (PTC).

Table 2
Input data for the solar collectors' models [72,86–88].

Parameter	Value
Collector aperture width (w_{ap})	4.0 m
Collector length (PTC-PV) (L_{PTC-PV})	45.0 m
Collector length (PTC) (L_{PTC})	90.0 m
Number of collectors (N_c)	2
Absorber tube diameter (D_{tub})	50.0 mm
Absorber tube thickness (δ_{tub})	2.0 mm
Absorber tube emissivity (ε_{tub})	0.2
Absorber tube absorptance (α_{tub})	0.97
Absorber tube thermal conductivity (k_{tub})	0.205 kW/(m K)
Glass cover thickness (δ_{cov})	3.0 mm
Glass cover emissivity (ε_{cov})	0.86
Glass cover absorptance (α_{cov})	0.02
Glass cover transmittance (τ_{cov})	0.96
Glass cover optical efficiency ($\eta_{opt,cov}$)	80 %
Glass cover thermal conductivity (k_{cov})	0.011 kW/(m K)
Air gap thickness (δ_{air})	20.0 mm
PV cell thickness (δ_{PV})	0.3 mm
PV cell emissivity (ε_{PV})	0.2
PV cell absorptance (α_{PV})	0.35
PV cell transmittance (τ_{PV})	0.6
PV thermal conductivity (k_{PV})	0.05 kW/(m K)
PCE of PV cell at 25 °C (η_{PV})	24.7 %
Direct Normal Irradiance (I_b)	0.8 kW/m^2
Ambient temperature (T_{amb})	25 °C
Sky temperature (T_{sky})	25 °C
Sun Temperature (T_{sun})	5,770 K
Working pressure (P_{HTF})	300 kPa
Solar incident angle (θ)	0 °
Wind velocity	3 m/s

Table 3
Input data for the double-stage vapor compression-absorption cascade system [47,48,52,90].

Parameter	Value
Cooling capacity ($\dot{Q}_{cool}$)	85 kW
Maximum solution concentration ($X_{14''}$)	61 %
Condensation temperature ($T_{20''}$)	25 °C
Condensation mass flow rate ($\dot{m}_{cond}$)	5 kg/s
Evaporation temperature ($T_{31''}$)	−15 °C
Evaporation mass flow rate ($\dot{m}_{eva}$)	3 kg/s
Solution heat exchanger efficiency (η_{SHX1}, η_{SHX2})	70 %
Delta T in High desorber (ΔT_{hd})	5 K
Absorber Pinch Point (PP_{abs})	5 K
High condenser – low desorber Pinch Point (PP_{hc-ld})	3 K
Low condenser Pinch Point (PP_{cond})	5 K
Evaporator Pinch Point (PP_{eva})	5 K
Internal heat exchanger efficiency (η_{IHX})	50 %
Temperature lift (ΔT_{lift})	45 K
Subcooling degree in suction line	5 K
Superheated degree in liquid line	5 K
Cascade HX degree of overlap temperature (ΔT_{OT})	5 K
Compressor isentropic efficiency ($\eta_{s,co}$)	80 %
Compressor electromechanical efficiency ($\eta_{em,co}$)	90 %

The solar field is configured with two rows connected in parallel, each composed of a PTC-PV collector followed in series by a conventional PTC. The total solar collecting area amounts to 1,080 m^2. The thermal behaviour of each collector receiver is modelled using a thermal resistance analogy under steady-state and thermodynamic equilibrium assumptions, with solar radiation considered uniformly distributed across the receiver surface. Table 2 outlines the key design parameters and boundary conditions applied in the model. Therminol-66 is selected as the Heat Transfer Fluid (HTF), due to its suitability for the required temperature range, low relative pressure, and thermal stability (see Table A2).

2.3. Refrigeration system

An additional innovation of this study is the integration of a double-stage vapor compression–absorption cascade refrigeration system designed to deliver low-temperature cooling between −5 °C and −30 °C. This configuration integrates two thermodynamic cycles connected through a cascade heat exchanger, functioning as the evaporator in the absorption cycle and the condenser in the vapor compression cycle. To utilise the high-temperature thermal energy from the solar field efficiently, a double-effect absorption cycle is adopted, enhancing the system's COP. Although series flow configurations typically offer higher cooling capacity, this work employs a parallel-flow double-effect water/lithium bromide absorption cycle, which maintains a high COP while simplifying system integration [90]. The risk of LiBr crystallisation due to fluctuations on solar irradiance has been accounted for by limiting the solution concentration to 61 % and by buffering variations in solar input via the thermal storage tank, consistent with standard industrial controls that prevent supersaturation in the desorber.

The proposed vapor compression system operates on a single-stage cycle integrated with an Internal Heat Exchanger (IHX). The IHX improves system efficiency by subcooling the refrigerant before expansion and superheating it before compression—particularly effective when the temperature lift (difference between condensation and evaporation temperatures) ranges from 40 to 60 K [91,92]. n-Pentane (R-601) is selected as the working fluid due to its favourable thermodynamic properties and minimal environmental impact [93], including zero ozone depletion potential (ODP) and very low global warming potential (GWP), below 20. However, n-pentane is highly flammable (flash point − 49 °C), which necessitates careful safety considerations in industrial systems. Standard measures include using hermetically sealed compressors and piping, leak detection systems, and explosion-proof electrical components in compliance with international safety standards (e.g., IEC 60079, EN 378). In single-stage cycles with IHX, n-pentane has demonstrated higher COPs than alternatives like R245fa [92]. Within the cascade heat exchanger, superheated vapor from the compressor (state 25 to 26) transfers heat to the absorption cycle and condenses at a lower temperature managed by the absorption loop. The temperature difference between the evaporating medium of the absorption side and the condensing refrigerant of the compression side in the cascade condenser is defined as the degree of overlap (ΔT_{OT}) [45].

A 31-state thermodynamic model is developed for the cascade refrigeration system, with each state defined by key parameters such as temperature, pressure, enthalpy, mass flow rate, and fluid composition. In addition to applying mass and energy conservation laws, the UA-LMTD method is used to characterise the heat exchange processes involving external streams—namely, the absorber, low-temperature condenser, and evaporator—following the approach of Herold [90]. This method allows heat exchanger performance and sizing to be effectively estimated using a single parameter, under the assumption that UA remains relatively stable throughout each process.

The following modelling assumptions are made: (*i*) the system operates under steady-state conditions; (*ii*) pressure drops and heat losses in pipelines and heat exchangers are neglected; (*iii*) LiBr-H_2O mixtures in both absorber and desorber are assumed to be in thermodynamic equilibrium at specified pressure and temperature; (*iv*) expansion processes are considered isenthalpic; (*v*) temperature difference between the inlet and outlet in the high desorber ($\Delta T_{hd} = T_{4'} - T_{5'}$) is fixed; (*vi*) both the absorber and low-temperature condenser are water-cooled; (*vii*) compression is adiabatic but non-isentropic; and (*viii*) specific states (1, 4, 8, 11, 14, and 18) are assumed to be saturated liquid, while state 10 is considered saturated vapor. Subcooling and superheating are included in the compression cycle due to thermal exchanges in the liquid and suction lines. Input data for the model are summarised in Table 3.

Table 4
Input data for the PEM electrolyser model [94–98].

Parameter	Value
Membrane thickness, Nafion 117 (δ_m)	175 μm
Membrane water content (λ_m)	14
Area of single-cell polar plate (A_{cell})	0.05 m^2
Number of cells (n_c)	50
Transfer coefficient of the anode (α_a)	1.5
Transfer coefficient of the cathode (α_c)	0.5
Exchange current density, anode Pt-Ir catalyst ($J_{0,a}$)	10^{-7} A/cm^2
Exchange current density, cathode Pt catalyst ($J_{0,c}$)	10^{-3} A/cm^2
Activation energy, anode ($E_{act,a}$)	76 kJ/mol
Activation energy, cathode ($E_{act,c}$)	18 kJ/mol
Power input as Fraction of $\dot{W}_{el,ORC}$(Fr_{PEM})	0.25
Operating temperature (T_{PEM})	80 °C
Operating pressure (P_{PEM})	101.3 kPa
Lower heating value of hydrogen (LHV_{H2})	120 MJ/kg

2.4. Electrolyser

The PEM electrolyser is a widely adopted technology for hydrogen production in energy systems utilising low-grade heat sources [94,95]. During the electrolysis process, both electricity and heat are required to drive the electrochemical reactions. In this system, the electrical power needed to meet the electrolyser's energy demands is supplied by the output of the ORC turbine. To match operational conditions, ambient-temperature liquid water is preheated via a heat exchanger before entering the PEM electrolyser, ensuring optimal performance and efficiency in hydrogen generation.

Water is introduced at the anode side of the PEM electrolyser, where it splits into oxygen, protons, and electrons. Under the influence of the applied electric current, the protons migrate through the polymer electrolyte membrane and are reduced at the cathode by electrons from the external circuit, resulting in the formation of hydrogen gas. The produced hydrogen is then cooled to ambient temperature, compressed, and stored for later use as fuel. Concurrently, oxygen generated at the anode is separated from the water/oxygen mixture and also cooled to the ambient reference temperature. The remaining warm water is recirculated back into the feed stream for use in the next electrolysis cycle. The fixed parameters used in the PEM electrolyser model are listed in Table 4.

3. System modelling

The thermodynamic evaluation of the proposed polygeneration system is carried out using both the First and Second Laws of Thermodynamics. This involves applying mass, energy, and exergy balance equations to each system component, assuming steady-state operation as the study focuses on the thermodynamic performance under typical design and operating conditions rather than on transient behaviour. The effects of pipeline pressure drops and heat losses are neglected because preliminary estimations showed that their magnitudes are small compared to the overall system pressure and energy flows, and thus have a negligible influence on the main performance indicators.

The system is divided into subsystems, including the solar system, ORC, compression-absorption cascade system, and PEM electrolyser. The thermodynamic inlet and outlet states of each component are determined using the Engineering Equation Solver (EES) software, based on specified input data and underlying assumptions.

3.1. Energy and exergy analysis relations

The general mass and energy balance equations for each component are expressed as follows:

$$\sum_{in}\dot{m}_{in}-\sum_{out}\dot{m}_{out}=0 \tag{1}$$

$$\sum_{in}h_{in}\dot{m}_{in}-\sum_{out}h_{out}\dot{m}_{out}+\dot{W}+\dot{Q}=0 \tag{2}$$

Using the Second Law of Thermodynamics, the exergy analysis of the polygeneration system can be performed to determine the maximum extractable work when the system is in equilibrium with the environment (i.e., dead state). The general exergy balance for a control volume can be expressed as follows:

$$\sum_{j}\left(1-\frac{T_0}{T_j}\right)\dot{Q}_j+\dot{W}+\sum_{in}\dot{m}_{in}ex_{in}-\sum_{out}\dot{m}_{out}ex_{out}-\dot{E}x_d=0 \tag{3}$$

where $\dot{E}x_d$ and ex represent the exergy destruction rate and exergy per unit mass flow rate, respectively. $\dot{Q}_j$ denotes the heat transfer rate across the component boundary at temperature T_j at state j, and $\dot{W}$ is the work rate. The subscript 0 indicates that the property is evaluated at environmental or dead state conditions.

When excluding the effects of electricity, magnetism, surface tension and nuclear reaction, the total exergy of a system can be categorised into four distinct parts: physical exergy, kinetic exergy, potential exergy, and chemical exergy [99]. This study focuses exclusively on the physical and chemical components of exergy.

$$\dot{E}x=\dot{E}x^{ph}+\dot{E}x^{ch} \tag{4}$$

The physical exergy per unit mass flow rate, $\dot{E}x^{ph}$, at a specific state is defined as follows [100]:

$$\dot{E}x^{ph}=\dot{m}[(h-h_0)-T_0(s-s_0)] \tag{5}$$

For subsystems with no change in fluid composition, like the solar system and ORC, the calculation of chemical exergy is not required, as it remains constant. However, for both the refrigeration system and the PEM electrolyser, the chemical energy must be considered. The LiBr-H_2O solution in the absorption loop of the cascade refrigeration system, the chemical exergy per mas flow rate, $\dot{E}x^{ch}$, at a given state is calculated following the method outlined by [101,102]:

$$\dot{E}x^{ch}=\dot{m}\left[\sum_i X_i\left(\mu_{i,0}-\mu^*_{i,0}\right)\right] \tag{6}$$

where $\mu_{i,0}$ (kJ/kg) represents the chemical potential of component "i" at the dead state pressure and temperature, corresponding to the composition at a given state; $\mu^*_{i,0}$ (kJ/kg) denotes the chemical potential of component "i" at dead state conditions when the system has reached chemical equilibrium with the environment; and X_i is the mass fraction of component "i". On the other hand, the chemical exergy of hydrogen under standard conditions is approximately 236.09 kJ/mol [103], while the specific chemical exergy of biomass at the same conditions is estimated to be around 18.75 kJ/kg [104].

A system is considered to be in thermodynamic equilibrium with its environment when thermal, mechanical, and chemical equilibria are simultaneously achieved [105]. Since all working fluids in each defined subsystem are confined, they cannot maintain pressure or compositional balance with the environment. In this case, Gaggioli [106] suggests defining the dead state as the condition achieved when the system is shut down and has reached thermal equilibrium with the surroundings.

Following the methodology previously proposed by the authors [60,101], the ambient temperature (T_0 = 25 °C) is adopted as the reference dead-state temperature for all subsystems. However, each subsystem is assigned a specific dead-state pressure, tailored to its thermodynamic characteristics (see Table A3):

- For the solar field, the dead-state pressure is selected as an intermediate value between the HTF operating pressure and atmospheric pressure, and is set to $P_{0,sol} = 150$ kPa.
- For both the ORC and the vapor compression refrigeration cycle, the dead-state pressure ($P_{0,ORC}$, $P_{0,VCRC}$) corresponds to the saturation pressure of the respective working fluid — toluene and n-pentane — at the designated reference temperature T_0.
- Within the absorption loop of the cascaded refrigeration system, the dead-state pressure is defined to match the pressure at state 1', such that $P_{0,VARC} = P_{1'}$. The corresponding LiBr solution composition at dead state is calculated assuming chemical equilibrium, denoted as $X_{0,LiBr}\left(T_{0,VARC}, P_{0,VARC}\right)$.
- In the case of the PEM electrolyser, which is designed to operate at atmospheric pressure, the dead-state pressure is taken as $P_{0,PEM} =$ 101.3 kPa.

The following subsections present the detailed modelling of the solar subsystem and PEM electrolyser.

3.1.1. Modelling of solar collectors

The energy formulations for both the PTC-PV and PTC are based on the equations presented by Forristal [88] and correlations described by Incropera and DeWitt [107] for a tubular receiver with a glass cover, as shown in Figs. 4 and 5. A steady-state energy balance is proposed for the absorber tube cross-section in each type of collector, applying the energy conservation principle to each surface within the section.

To simplify the model, solar absorption by the glass cover is represented as a heat flux, with an estimated optical efficiency employed to calculate the absorbed solar energy. This relationship is expressed by the following equation:

$$\dot{q}_{sol,cov} = I_b w_{ap} \eta_{opt,cov} \alpha_{cov} \tag{7}$$

where $\eta_{opt,cov}$ represents the effective optical efficiency at the glass cover considering multiple factors like shadowing, geometry errors and dirtiness.

For the PTC-PV, the solar energy absorbed by the PV layer is also treated as a heat flux and can be calculated as follows:

$$\dot{q}_{sol,PV} = I_b w_{ap} \eta_{opt,cov} \tau_{cov} \alpha_{PV} \tag{8}$$

Likewise, the solar energy absorbed by the absorber tube is expressed as:

$$\dot{q}_{sol,tub}^{PTC-PV} = I_b w_{ap} \eta_{opt,cov} \tau_{cov} \tau_{PV} \alpha_{tub} \tag{9}$$

In the case of the PTC, a similar approach is applied:

$$\dot{q}_{sol,tub}^{PTC} = I_b w_{ap} \eta_{opt,cov} \tau_{cov} \alpha_{tub} \tag{10}$$

The conduction heat transfer through the absorber tube and the glass cover is calculated as follows, assuming a constant conduction heat transfer coefficient, which is evaluated at the average temperature between the inner and outer surfaces. According to Fourier's law of conduction through a cylinder:

$$\dot{q}_{cnd,tub} = 2\pi k_{tub}\left(T_{tub,e} - T_{tub,i}\right) \Big/ \ln\left(D_{tub,i}/D_{tub,e}\right) \tag{11}$$

$$\dot{q}_{cnd,cov} = 2\pi k_{cov}\left(T_{cov,i} - T_{cov,e}\right) \Big/ \ln\left(D_{cov,e}/D_{cov,i}\right) \tag{12}$$

$$\dot{q}_{cnd,PV} = 2\pi k_{PV}\left(T_{PV,i} - T_{PV,e}\right) \Big/ \ln\left(D_{PV,e}/D_{PV,i}\right) \tag{13}$$

The convective heat transfer from the inner surface of the absorber tube to the HTF is determined using Newton's law of cooling:

$$\dot{q}_{HTF} = ht_{HTF} D_{tub,i} \pi \left(T_{tub,i} - T_{HTF}\right) \tag{14}$$

The fluid heat transfer coefficient, h_{HTF}, is calculated using the Dittus-Boelter correlation for the turbulent flow region, in which all physical properties of the HTF are evaluated at the mean bulk temperature.

$$Nu_{HTF} = 0.023 Re^{\frac{4}{5}} Pr^{\frac{2}{5}} \tag{15}$$

The heat losses in the collectors primarily occur from the glass cover to the atmosphere through convection and radiation thermal mechanisms. The radiation heat transfer between the PV layer, in the case of PTC-PV, or the absorber, in the case of PTC, and the glass cover is calculated using the following equation:

$$\dot{q}_{rad,PV} = \frac{\sigma \pi D_{PV,e}\left({T_{PV}}^4 - {T_{cov,i}}^4\right)}{\left(1/\varepsilon_{PV} + (1-\varepsilon_{cov}) D_{PV}/\varepsilon_{cov}\left(D_{cov,i}\right)\right)} \tag{16}$$

$$\dot{q}_{rad,tub} = \frac{\sigma \pi D_{tub,e}\left({T_{tub}}^4 - {T_{cov,i}}^4\right)}{\left(1/\varepsilon_{tub} + (1-\varepsilon_{cov}) D_{tub,e}/\varepsilon_{cov}\left(D_{cov,i}\right)\right)} \tag{17}$$

The convection heat transfer from the glass cover to the atmosphere is assumed to be forced by wind conditions and represents the largest source of heat loss. According to Newton's law of cooling:

$$\dot{q}_{cnv,cov} = ht_{cnv,cov} D_{cov,e} \pi \left(T_{cov,e} - T_{sky}\right) \tag{18}$$

In this case, the Nusselt number is estimated using Zukauskaśs correlation [108], which applies to external forced convection flow perpendicular to an isothermal cylinder.

Radiative heat transfer arises due to the temperature difference between the glass cover and the sky. The net radiation exchange is calculated using the following expression:

$$\dot{q}_{rad,cov} = \sigma D_{cov,e} \pi \varepsilon_{cov}\left({T_{cov,e}}^4 - {T_{sky}}^4\right) \tag{19}$$

For the PTC-PV, the electrical power generated by PV cells is calculated using the following equation:

$$\dot{W}_{el,PV} = I_b A_{PV}\left(\eta_{opt,cov}\tau_{cov}\right)\eta_{PV} \tag{20}$$

The PCE of the PV cell, η_{PV}, must be calculated across the operating conditions. To date, very little work has been paid to evaluating PSC performance under variable operating conditions to determine the temperature coefficient for maximum power (T_{PCE}). For this study, a T_{PCE} of −0.037 rel %/°C in the range of 300–500 K was selected based on the results provided by Abedini-Ahangarkola et al. [109], who analysed a high-efficiency PSC with three active layers.

$$\eta_{PV} = 24.7 - 0.037(T_{PV} - 300)/100 \tag{21}$$

The thermal efficiency of the solar collectors, accounting for all the aforementioned types of thermal losses, is defined as the ratio of the useful energy absorbed to the available solar irradiance:

$$\eta_{PTC-PV} = \eta_{PTC-PV,th} + \eta_{PTC-PV,el} = \frac{\dot{q}_u^{PTC-PV}}{\dot{q}_{sol}} = \frac{\left[\dot{m}_{HTF} Cp_{HTF}(T_{7'} - T_{6'}) + \dot{W}_{el,PV}\right] \Big/ L_{PTC-PV}}{I_b w_{ap}} \tag{22}$$

$$\eta_{PTC} = \frac{\dot{q}_u^{PTC}}{\dot{q}_{sol}} = \frac{\left[\dot{m}_{HTF} Cp_{HTF}(T_{8'} - T_{7'})\right] \Big/ L_{PTC}}{I_b w_{ap}} \tag{23}$$

The storage tank enables the accumulation of thermal energy, ensuring a continuous and reliable energy supply despite fluctuations in solar irradiance. The energy balance produced in the thermal energy storage tank is determined by the following equation

$$\frac{d(m_{HTF} Cp_{HTF} T)}{dt} = \dot{Q}_{in} - \dot{Q}_{out} - \dot{Q}_{loss} \tag{24}$$

From literature review [63], a cylindrical storage tank separated into three mixing zones is assumed, with its volume estimated as the total solar collecting area divided by 80. The tank is designed with equal diameter and height, and a uniform thermal oil temperature is considered throughout each mixing zone. The overall heat loss coefficient (U_{st}) is taken as 0.5 W/m^{2}K.

Assuming steady-state conditions, where the storage tank does not accumulate thermal energy, Eq. (24) can be reformulated for each mixing zone by equating the useful heat input from the PTCs to the sum of the heat transferred to the ORC and the thermal losses to the ambient, i.e.,

$$\dot{m}_{HTF}Cp_{HTF}\left(T_{8'}-T_{st,1}\right)=\dot{m}_{HTF}Cp_{HTF}\left(T_{st,1}-T_{st,2}\right)+U_{st}A_{st,1}\left(T_{st,1}-T_{amb}\right) \tag{25}$$

$$\dot{m}_{HTF}Cp_{HTF}\left(T_{st,1}-T_{st,2}\right)=\dot{m}_{HTF}Cp_{HTF}\left(T_{st,2}-T_{st,3}\right)+U_{st}A_{st,2}\left(T_{st,2}-T_{amb}\right) \tag{26}$$

$$\dot{m}_{HTF}Cp_{HTF}\left(T_{st,2}-T_{st,3}\right)=\dot{m}_{HTF}Cp_{HTF}\left(T_{st,3}-T_{5'}\right)+U_{st}A_{st,3}\left(T_{st,3}-T_{amb}\right) \tag{27}$$

Furthermore, it is important to note the collector field inlet temperature is assumed equal to the third zone of the storage tank ($T_{10'}=T_{st,3}$), while the outlet temperature to the ORC evaporator corresponds to the first zone ($T_{9'}=T_{st,1}$).

3.1.2. Modelling of PEM electrolyser

From the thermodynamic viewpoint, the energy required to drive the water splitting reaction is given by the change in enthalpy

$$\Delta H=\Delta G+T\Delta S \tag{28}$$

where ΔG is the electrical energy demand (change in Gibb's free energy) and $T\Delta S$ is the thermal energy demand.

The most common way to represent the performance of a PEM electrolyser is through the polarisation curve, which illustrates the relationship between cell current density (J) and voltage (V). This relationship corresponds to the electrical input supplied to the electrolyser, defined as follows [95]

$$\dot{W}_{el,PEM}=JV \tag{29}$$

$\dot{W}_{el,PEM}$ is an input of the model, which is determined by a fraction (Fr_{PEM}) of the power generated by the ORC turbine ($\dot{W}_{el,ORC}$). The PEM electrolyser voltage can be expressed as

$$V=V_0+V_{act,a}+V_{act,c}+V_{ohm} \tag{30}$$

where, V_0 is the reversible potential and is obtained by the Nernst equation

$$V_0=1.229-8.5\times10^{-4}(T_{PEM}-298) \tag{31}$$

Here, $V_{act,a}$, $V_{act,c}$, and V_{ohm} are the anode activation overpotential, the cathode activation overpotential and the ohmic overpotential of the electrolyte, respectively. The activation over-potential losses ($V_{act,i}$) is given by [110]

$$V_{act,i}=\frac{RT}{\alpha_i zF}\ln\left(\frac{J}{J_{0,i}}\right),i=a,c \tag{32}$$

where F is the Faraday constant, R is the universal gas constant, α is the charge transfer coefficient, and J_0 is the exchange current density of the electrolyser which can be obtained through an Arrhenius expression [111]. In water electrolysis, z = 2.

$$J_{0,i}=J_i^{ref}exp\left[-\frac{E_{act,i}}{R}\left(\frac{1}{T}-\frac{1}{T_{ref}}\right)\right],i=a,c \tag{33}$$

where E_{act} is defined as the activation energy for the electrode reaction, and J_i^{ref} is the exchange current density at a known temperature (T_{ref}).

The ohmic over-potential of the electrolyte is caused mainly by the ionic resistance of the membrane to the protons transported through it. The local ionic conductivity (σ_{PEM}) of the electrolyser membrane has been empirically determined as [112]

$$\sigma_{PEM}=(0.5139\lambda_m-0.326)exp\left[1268\left(\frac{1}{303}-\frac{1}{T}\right)\right] \tag{34}$$

where λ represents the water content of the membrane. For a membrane thickness δ_m, the ohmic overpotential is

$$V_{ohm}=J\frac{\delta_m}{\sigma_{PEM}} \tag{35}$$

According to Faraday's law, the outlet molar flow rates of the PEM electrolyser can be determined as follows

$$\dot{n}_{H_2,out}=\frac{n_cJ}{2F}\eta_F \tag{36}$$

$$\dot{n}_{O_2,out}=\frac{n_cJ}{4F}\eta_F \tag{37}$$

$$\dot{n}_{H_2O,out}=\dot{n}_{H_2O,in}-\frac{n_cJ}{2F}\eta_F \tag{38}$$

The inlet flow rate of H_2O is considered a known parameter of the model, i.e., $\dot{n}_{H_2O,in}=1.25\frac{n_cJ}{2F}\eta_F$ [111]. n_c is the number of stacked electrolytic cells. The Faraday's efficiency (η_F) is taken as $\eta_F=0.99$. This value is consistent with experimental results reported for commercial low-temperature PEM systems operating under moderate current densities ($\leq$ 2 A cm^{-2}) and near-ambient pressures [94,113,114]. Within this operating range, η_F remains nearly constant, as gas crossover and parasitic losses are negligible. Since the present study focuses on steady-state operation around the nominal load, adopting a fixed efficiency introduces minimal deviation in the predicted hydrogen production rate. However, for conditions involving dynamic operation or extended current density ranges, the Faraday efficiency could be expressed as a function of current density, as proposed in [115], which may be considered in future model refinements.

The thermal efficiency of the PEM electrolyser can be expressed as

$$\eta_{en,PEM}=\frac{\dot{Q}_{H_2}}{\dot{W}_{el,PEM}+\dot{Q}_{heat,H_2O}}=\frac{\dot{n}_{H_2,out}LHV_{H2}}{\dot{W}_{el,PEM}+\dot{Q}_{heat,H_2O}} \tag{39}$$

where LHV_{H2} is the lower heating value of H_2 and Q_{heat,H_2O} is the rate of thermal energy input to the heat exchanger for heating up the H_2O.

3.2. Performance indexes

This section outlines the performance evaluation of the poly-generation system. Eqs. 40–41 define the energy and exergy efficiency ratios for the net electricity output from the ORC. In Eq. (41), the Petela model [116] is applied to calculate the exergy flow of the incoming solar irradiation

$$\eta_{en,el}=\frac{\dot{W}_{el,ORC}-\dot{W}_{ORC,pump}}{\dot{Q}_{sol}+\dot{Q}_{bh}} \tag{40}$$

$$\eta_{ex,el}=\frac{\dot{W}_{el,ORC}-\dot{W}_{ORC,pump}}{\dot{E}x_{in}} \tag{41}$$

where

$$\dot{W}_{el,ORC}=\dot{m}_{ORC}h_8-\dot{m}_{ORC,A}h_{10}-\dot{m}_{ORC,B}h_9 \tag{42}$$

$$\dot{W}_{ORC,pump}=\dot{m}_{ORC,A}(h_2-h_1)+\dot{m}_{ORC}(h_5-h_4) \tag{43}$$

$$\dot{Q}_{sol} = I_b w_{ap}(L_{PTC} + L_{PTC-PV})N_c \tag{44}$$

$$\dot{Q}_{bh} = \frac{\dot{m}_{HTF}(h_{1'} - h_{11''})}{\eta_{bh}} \tag{45}$$

$$\dot{E}x_{in} = \dot{Q}_{sol}\left[1 - \frac{4}{3}\left(\frac{T_0}{T_{sun}}\right) + \frac{1}{3}\left(\frac{T_0}{T_{sun}}\right)^4\right] + \dot{m}_{bio}\dot{E}x_{bio} \tag{46}$$

where η_{bh} is the thermal efficiency of the biomass heater, which is assumed to be 85 %.

The energy and exergy efficiency ratios of the polygeneration system are defined as follows

$$\eta_{en,poly} = \left[\frac{\left(\dot{W}_{el,ORC} + \dot{W}_{el,PV} + \dot{Q}_{H_2} + \dot{Q}_{heat} + \dot{Q}_{cool}\right) - \dot{W}_{el,PEM} - \dot{W}_{el,co} - \dot{W}_{ORC,pump} - \dot{W}_{S,pump}}{\dot{Q}_{sol} + \dot{Q}_{bh}}\right] \tag{47}$$

$$\eta_{ex,poly} = \left[\frac{\left(\dot{W}_{el,ORC} + \dot{W}_{el,PV} + \dot{E}_{P,PEM} + \dot{E}_{P,heat} + \dot{E}_{P,cool}\right) - \dot{W}_{el,PEM} - \dot{W}_{el,co} - \dot{W}_{ORC,pump} - \dot{W}_{S,pump}}{\dot{E}x_{in}}\right] \tag{48}$$

where

$$\dot{W}_{el,co} = \dot{m}_{VCRC}(h_{25''} - h_{24''}) \tag{49}$$

$$\dot{Q}_{heat} = \dot{m}_{heat}(h_{14} - h_{13}) \tag{50}$$

$$\dot{Q}_{cool} = \dot{m}_{eva}(h_{30''} - h_{31''}) \tag{51}$$

$$\dot{W}_{S,pump} = \dot{m}_{VARC,1}(h_{2''} - h_{1''}) + \dot{m}_{VARC,2}(h_{12''} - h_{11''}) \tag{52}$$

$$\dot{E}_{P,PEM} = \dot{E}x_{5'''} + \dot{E}x_{6'''} \tag{53}$$

$$\dot{E}_{P,heat} = \dot{E}x_{14} - \dot{E}x_{13} \tag{54}$$

$$\dot{E}_{P,cool} = \dot{E}x_{30''} - \dot{E}x_{31''} \tag{55}$$

The COP of the entire compression-absorption cascade system, along with those of the individual sub-cycles—VCRC and VARC—can be explicitly expressed as follows:

$$COP_{VCRC} = \frac{\dot{Q}_{cool}}{\dot{W}_{el,co}} \tag{56}$$

$$COP_{VARC} = \frac{\dot{Q}_{cas}}{\dot{Q}_{hd} + \dot{W}_{S,pump}} \tag{57}$$

$$COP_{cas} = \frac{\dot{Q}_{cool}}{\dot{W}_{el,co} + \dot{Q}_{hd} + \dot{W}_{S,pump}} \tag{58}$$

where $\dot{Q}_{hd}$ and $\dot{Q}_{cas}$ are the rate of heat input to the high desorber and cascade heat exchanger, respectively, which are calculated by

$$\dot{Q}_{hd} = \dot{m}_{HTF}(h_{4'} - h_{5'}) \tag{59}$$

$$\dot{Q}_{cas} = \dot{m}_{VCRC}(h_{26''} - h_{25''}) \tag{60}$$

To evaluate the exergy performance of specific components and subsystems z of the polygeneration system, additional parameters are determined using component-level exergy balances based on the fuel–product formulation [117].

$$\dot{E}_{F,z} - \dot{E}_{P,z} = \dot{E}_{D,z} - \dot{E}_{L,z} \tag{61}$$

$$\eta_{ex,z} = \frac{\dot{E}_{P,z}}{\dot{E}_{F,z}} \tag{62}$$

where $\dot{E}_{F,z}$ corresponds to the fuel exergy, $\dot{E}_{P,z}$ is the product exergy, $\dot{E}_{D,z}$ is the destroyed exergy, and $\dot{E}_{L,z}$ is the exergy loss. The only exergy loss of the complete system is attributable to compression-absorption cascade refrigeration subsystem as the waste heat generated in the absorber and condenser is assumed to be unusable. The corresponding exergy balance for each subsystem is presented in Table A4.

The exergy destruction ratio ($Y_{D,k}$) relates the exergy destroyed in component k to the total fuel exergy of the system and is defined as follows:

$$Y_{D,k} = \frac{\dot{E}_{D,k}}{\dot{E}x_{in}} \tag{63}$$

The irreversibility ratio of component k, which expresses the proportion of exergy destruction in component k relative to the total exergy destruction in the system, is defined as follows:

$$Y^*_{D,k} = \frac{\dot{E}_{D,k}}{\dot{E}_{D,tot}} \tag{64}$$

3.3. Financial model

The financial modelling for the polygeneration system entails a comprehensive evaluation of capital investments, operating costs, and revenue streams over the plant's economic life. The model aims to assess the financial feasibility of the project using standard investment appraisal metrics.

The total system cost is composed of the fixed initial investment costs, including equipment, installation and project development costs, and operation and maintenance costs. The cost balance equations for the kth component in the polygeneration system are expressed as follows [37,119,120]:

Table 5
Validation of the PTC-PV model.

Scenario		$\eta_{PTC-PV,th}$[%]	$\eta_{PTC-PV,el}$[%]	η_{PTC-PV}[%]	T_{HTF}[°C]
Scenario 1:	This study	55.75	10.34	66.09	325.80
[δ_{cov} = 2mm; δ_{air} = 5mm; η_{PV} = 15%]	Ref [72]	57.23	10.18	67.41	326.76
	Deviation	−2.6 %	1.6 %	−1.9 %	−0.3 %
Scenario 2:	This study	53.12	15.05	68.17	324.80
[δ_{cov} = 3mm; δ_{air} = 20mm; η_{PV} = 21%]	Ref [72]	55.02	14.87	69.89	325.85
	Deviation	−3.5 %	1.2 %	−2.5 %	−0.3 %
Scenario 3:	This study	55.81	11.89	67.69	325.80
[δ_{cov} = 4mm; δ_{air} = 40mm; η_{PV} = 17%]	Ref [72]	55.83	12.06	67.90	326.18
	Deviation	0.0 %	−1.4 %	−0.3 %	−0.1 %
Scenario 4:	This study	53.95	13.48	67.43	325.10
[δ_{cov} = 6mm; δ_{air} = 10mm; η_{PV} = 19%]	Ref [72]	55.77	13.25	69.03	326.16
	Deviation	−3.3 %	1.7 %	−2.3 %	−0.3 %

Table 6
Validation of the compression-absorption cascade refrigeration model.

Parameter	This study	Ref [52]	Deviation	Ref [55]	Deviation
$\dot{Q}_{hd}$[kW]	41.27	45.80	−9.9 %	45.10	−8.5 %
$\dot{Q}_{abs}$[kW]	70.34	72.63	−3.2 %	72.41	−2.9 %
$\dot{Q}_{cond}$[kW]	29.89	32.27	−7.4 %	32.15	−7.0 %
$\dot{W}_{el,cas}$[kW]	8.96	9.10	−1.5 %	9.46	−5.3 %
COP_{VARC}	1.43	1.29	10.9 %	1.31	9.2 %
COP_{VCRC}	5.58	5.49	1.6 %	5.28	5.7 %
COP_{cas}	0.99	0.91	8.8 %	0.92	7.6 %

$$\dot{Z}_k = CRF\left(\frac{Z_k\varphi}{t}\right) \tag{65}$$

$$CRF = \frac{r(1+r)^n}{(1+r)^n - 1} \tag{66}$$

$$\dot{C}_{tot} = \sum \dot{Z}_k \tag{67}$$

The component costs are given by Z_k, and are summarised in Table A5. The annual operating hours (t) and operating and maintenance cost coefficient (φ) are assumed to be 5000 h and 1.06, respectively. *CRF* describes the capital recovery factor, based on the discount rate (r) and the system's lifespan (n). The interest rate and the number of operation years in this work are assumed to be 10 % and 20 years.

The total investment cost (C_0) is defined as the summary of the Z_k. To estimate the investment cost of the heat exchangers, it is first necessary to determine their required heat transfer surface areas. This is accomplished using the following equation

$$\dot{Q}_{HX} = (UA)LMTD \tag{68}$$

Here, the variable $\dot{Q}_{HX}$ represents the heat transfer rate for a specific heat exchanger, while U denotes the overall heat transfer coefficient. Values for U are given in Table A6. A is the area of heat exchanger to be calculated, *LMTD* is the logarithmic mean temperature difference, which is calculated as follows

$$LMTD = \frac{\Delta T_1 - \Delta T_2}{ln\frac{\Delta T_1}{\Delta T_2}} \tag{69}$$

where,

$$\Delta T_1 = T_{hot,in} - T_{cold,out} \tag{70}$$

$$\Delta T_2 = T_{hot,out} - T_{cold,in} \tag{71}$$

In addition, the annual cash flow (*CF*) is determined as the net of annual inflows and outflows:

$$CF = R - O \tag{72}$$

where R represents the annual revenues generated from the generation of electricity, heat, cooling and hydrogen (see Table A7), and O encompasses annual operating expenses, including fuel from biomass backup, maintenance, labour, insurance, and administrative costs.

Provided that annual net cash flows are constant and the discount rate is uniform, the payback period (*PBP*) is calculated as [126]:

$$PBP = \frac{\ln\left(\frac{CF}{CF - C_0 r}\right)}{\ln(1+r)} \tag{73}$$

Due to the gradual decline in system performance caused by electro-mechanical and material degradation, the annual solar energy yield and net cash flows decrease over time. To account for this cumulative effect, a summation-based approach is applied. A 3 % year-over-year reduction in solar energy yield is assumed for the first five years [127–129], followed by a 1 % annual decline for the remaining system lifetime [130,131].

The Net Present Value (*NPV*) is computed by discounting future cash flows to their present value using the selected discount rate r, typically reflecting the cost of capital [126].

$$NPV = -C_0 + \sum_{x=1}^{n} \frac{CF_x}{(1+r)^x} \tag{74}$$

The Internal Rate of Return (IRR) is the discount rate at which the *NPV* equals zero. It is found by using the built-in IRR function in Microsoft Excel. This approach accounts for non-constant yearly cash flows and does not require an explicit algebraic solution of the non-linear NPV equation.

4. Model validation

Unlike the ORC system and the PTC, which were previously validated by the authors [60], this section proposes the validation procedure for both the PTC-PV, the compression-absorption cascade refrigeration system, and the PEM electrolyser.

The validation of the PTC-PV model is conducted by comparing it with literature results from Yan et al. [72]. Certain input parameters of the proposed model have been adjusted to allow for a meaningful comparison with results reported in the literature, such as adjustments to the receiver tube dimensions and the mass flow rate. Accordingly, the boundary conditions are set as follows: mass flow rate of 0.3 kg/s, inlet temperature of 30 °C, and the concentration ratio of 100. Four different scenarios are evaluated by varying three design parameters: the glass cover thickness (2, 3, 4 and 6 mm), the air gap thickness (5, 10, 20, 40 mm), and PCE of PV cell (15, 17, 19 and 21 %). Furthermore, the Sieder-Tate correlation (Eq. (75) is proposed for the HTF convective heat transfer coefficient, which is applicable to laminar flow with a low Reynolds number and accounts for viscosity (μ) variation with temperature when the temperature difference between the surface and the fluid

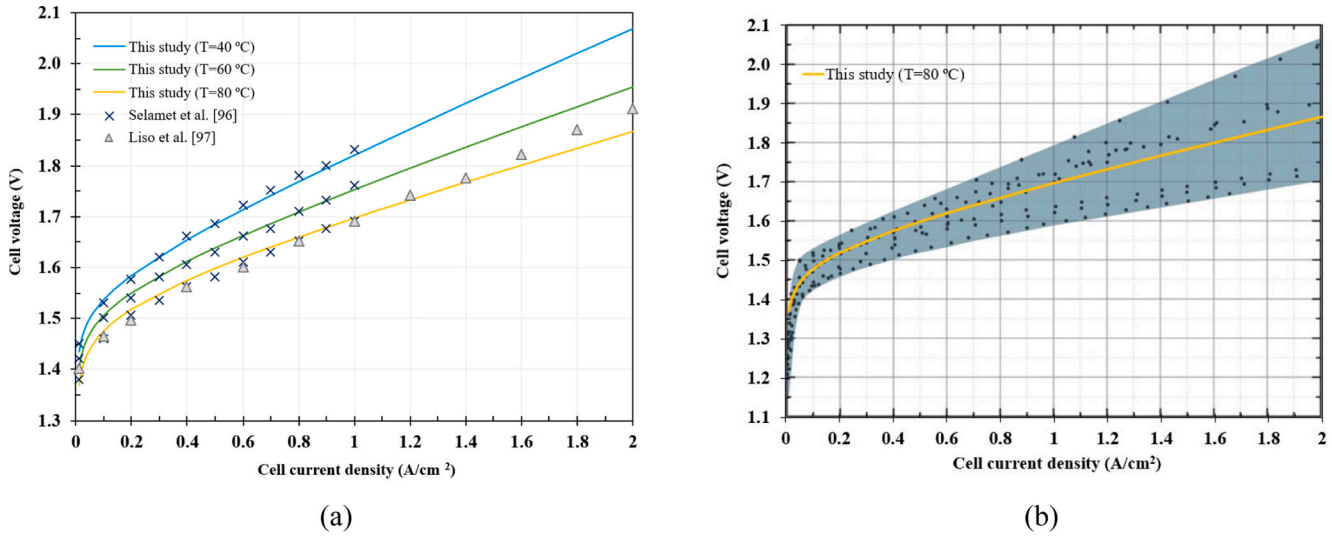

Fig. 6. Validation of PEM model: (a) with respect literature data [96,97]; (b) with respect several PEM electrolysers operating at 80 °C – copied from [94].

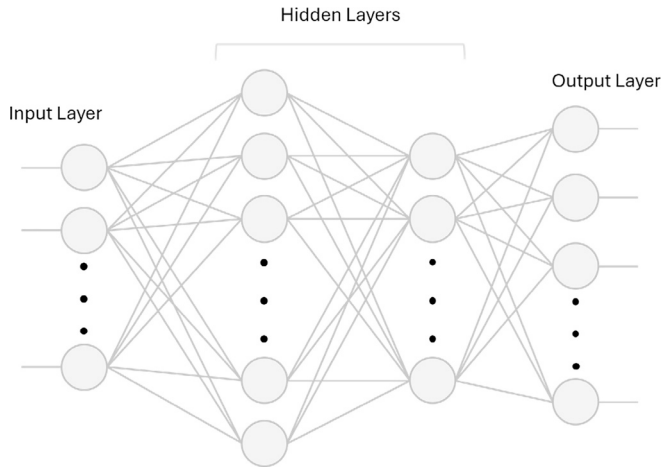

Fig. 7. Schematic diagram of multi-layer ANN.

is significant. All HTF properties are evaluated at the mean temperature of the fluid mass, except for $\mu_{abs,tub}$, which is evaluated at the absorber tube surface temperature.

$$Nu_{fl} = 1.86(RePrD/L)^{\frac{1}{3}}\left(\frac{\mu}{\mu_{abs,tub}}\right)^{0.14} \quad (75)$$

The comparison results presented in Table 5 indicate that the PTC-PV model aligns well with the findings reported in the referenced literature. The largest observed deviation, −3.5 % in thermal efficiency, can be mainly attributed to the thermal correlations used to estimate the heat loss coefficients.

The proposed model for the compression-absorption cascade refrigeration system is successfully validated using the data reported by Colorado and Rivera [52] and Mussati et al. [55]. Although both references utilise a series-flow double-stage absorption layout, they are used here as reference cases. For the validation of the results, the system's properties and operating conditions are assumed to be the same as those in the reference studies. Table 6 compares the model's output results with the numerical results reported in Refs. [52,55] for the analysed system operating with R134a in the VCRC and H_2O-LiBr in the VARC, and assuming the following inputs: $T_{31''} = -17°C$, $T_4 = 120.0°C$, and $\dot{Q}_{cool} = 50.0$ kW.

The observed deviation in the calculations is mainly attributed to the schematic configuration of the VARC. In general, parallel flow provides thermodynamic and heat transfer advantages over series flow, supporting the choice of the proposed design. Consequently, the proposed model shows good agreement with the simulation outcomes of the mentioned literature.

The developed model for the PEM electrolyser is validated using the set of experimental data reported by Selamet et al. [96] and Liso et al. [97]. Besides the fixed parameters shown in Table 4, the charge transfer coefficients (α_a, α_c) were calibrated to fit the model to the experimental data. These parameters are critical for accurately characterising the electrochemical reactions within an electrolyser and should not be treated as constant for a given electrode, as their variability enables more accurate prediction of PEM electrolyser performance under varying operating conditions [98]. As it can be seen in Fig. 6-a, the electrochemical response of the model is validated by comparing the obtained polarisation curves from the model and experiment at different temperatures. The modelling results align closely with the experimental data, demonstrating the accuracy of the proposed model. The minor deviation from the experimental curves can be attributed to simplifications and neglected factors in the model. Furthermore, the resulting polarisation curve was validated by comparing it with data from review papers. Fig. 6-b, adapted from [94], presents data for PEM electrolysers operating at 80 °C. The yellow line represents the I-V curve generated by the model developed in this study.

5. Optimisation of the system

The optimisation process carried out in this study is structured through a comprehensive and sequential methodology aimed at accurately capturing the complex relationships between design variables and system performance indicators. Based on the system modelling, six data inputs are selected as key decision variables for optimisation purpose, whereas the output layer comprises ten parameters representing the most crucial factors from the performance indexes, including system energy and exergy efficiencies, as well as various energy production indicators. A dataset comprising 3,000 samples from the input–output points is calculated with EES software and used to train the network.

The ANN is developed in MATLAB using the Levenberg–Marquardt backpropagation algorithm (*Trainlm*). This algorithm has shown fast convergence and high accuracy in function approximation tasks, providing excellent performance for regression problems with relatively low computational cost [56,59,132,133]. The network architecture consists of an input layer of six neurons, two hidden layers with 30 and

Table 7
Results from the exergy analysis of all system components.

Subsystem	Component	$\dot{W}$ or $\dot{Q}$ [kW]	$\dot{E}_F$[kW]	$\dot{E}_P$[kW]	$\dot{E}_D$[kW]	η_{ex}[%]	Y_D	Y^*_D	$\dot{Z}$[$/h]
Solar	PTC-PV	159.7 + 40.7	268.2	92.2	176.0	34.4	65.63	27.08	4.13
	PTC	414.1	536.3	145.6	390.7	27.1	145.70	60.13	4.30
	Storage tank	429.9	714.4	709.8	4.6	99.4	1.70	0.70	0.19
ORC	Superheater	22.1	7.7	6.9	0.8	89.6	0.30	0.12	0.04
	Evaporator	429.3	147.4	130.5	16.9	88.5	6.32	2.61	0.22
	Economiser	45.1	15.7	12.7	3.0	81.1	1.10	0.45	0.07
	Turbine	69.1	78.3	69.1	9.3	88.2	3.45	1.43	2.83
	Regenerator	58.2	40.4	39.2	1.2	96.9	0.46	0.19	0.04
	Recuperator	58.7	12.2	11.4	0.9	93.0	0.32	0.13	0.10
	PEM HX	0.2	0.3	0.1	0.3	21.8	0.09	0.04	0.01
	Heating HX	427.8	69.8	58.1	11.7	83.3	4.35	1.80	0.46
	Pump 1	0.3	0.3	0.2	0.1	74.9	0.03	0.01	0.04
	Pump 2	0.3	0.3	0.2	0.1	78.0	0.02	0.01	0.04
Cascaded refrigeration	High desorber	77.3	21.9	19.8	2.1	90.5	0.78	0.32	0.04
	High condenser – Low desorber	59.7	10.2	8.4	1.8	82.8	0.65	0.27	0.13
	Low condenser	54.0	2.8	0.0	2.8	0.0	1.04	0.43	0.04
	Cascade HX	106.4	5.9	3.2	2.6	54.9	0.98	0.41	0.19
	Absorber	129.7	7.3	0.0	7.3	0.0	2.73	1.13	0.13
	Solution HX 1	22.3	2.8	1.7	1.1	61.4	0.39	0.16	0.06
	Solution HX 2	18.4	4.3	3.2	1.0	75.7	0.39	0.16	0.06
	Compressor	23.8	23.8	21.4	2.4	90.0	0.89	0.37	1.09
	Internal HX	8.9	1.1	0.6	0.5	53.2	0.19	0.08	0.06
	Evaporator	85.0	17.7	8.7	9.0	49.2	3.35	1.38	0.16
Hydrogen	PEM Electrolyser	13.7	17.4	13.5	3.9	77.7	1.44	0.60	0.34
	Total	–	–	–	649.9	–	–	100.0	14.75

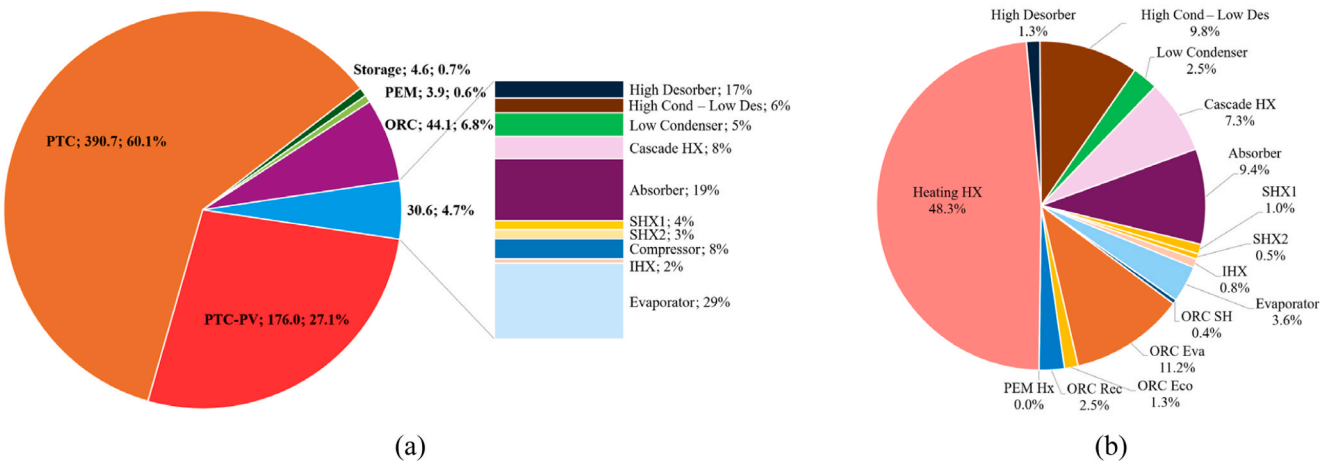

Fig. 8. (a) Exergy destruction rate and ratios of the components; (b) Distribution of the total heat transfer area.

20 neurons, respectively, and an output layer of ten neurons (see Fig. 7). The overall dataset is classified randomly into three subsets, i.e., training, testing, and cross-validation with 70 %, 15 %, and 15 % portions.

The most common criteria for assessing the networks performance are statistical error metrics, which quantify the difference between the network's predicted output ($\hat{y}$) and the actual target output (y). Here, both Mean Squared Error (*MSE*) and Coefficient of Determination (R^2) are considered. *MSE* measures the average squared deviation between predicted and actual values, whereas R^2 indicates the proportion of variance in the dependent variable that is explained by the independent variables.

$$MSE = \frac{1}{n}\sum_{i=1}^{n}(y_i - \hat{y}_i)^2 \tag{76}$$

$$R^2 = 1 - \frac{\sum_{i=1}^{n}(y_i - \hat{y}_i)^2}{\sum_{i=1}^{n}(y_i - \bar{y}_i)^2} \tag{77}$$

where $\bar{y}$ is the mean of the actual values.

Once trained, the ANN served as a fast surrogate model for system optimisation. The *gamultiobj* function in MATLAB, which utilises a genetic algorithm based on the NSGA-II framework, is used to carry out MOO. Two, or more, specific output variables can be selected as conflicting objectives, and the six inputs are varied within their original ranges. The optimum solutions for objective functions are represented by the Pareto frontier to illustrate the trade-offs between objectives. Finally, the optimal solution is selected using the TOPSIS (Technique for Order Preference by Similarity to Ideal Solution) decision-making method.

TOPSIS is a multi-criteria decision-making method that ranks

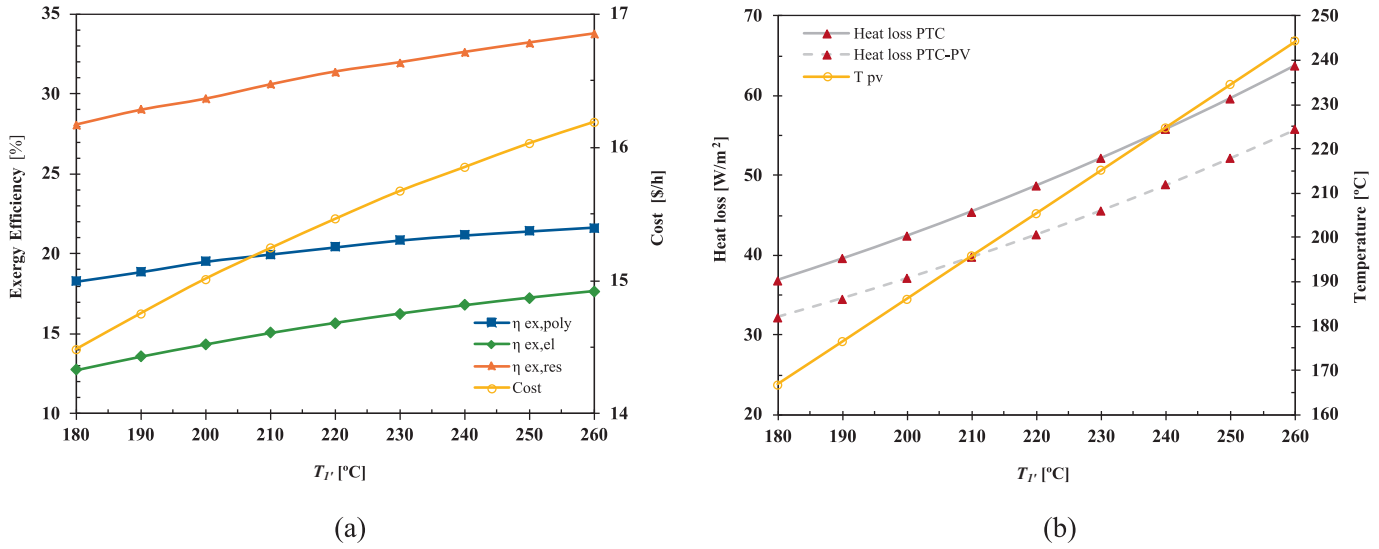

Fig. 9. Effect of ORC evaporator temperature on the system efficiency (a) and on the PTCs performance (b).

alternative solutions based on their relative closeness to an ideal solution. Technically, the method begins by normalizing all criteria to eliminate unit differences, followed by the identification of a positive ideal solution (best value for each criterion) and a negative ideal solution (worst value). Each alternative is then evaluated by calculating its Euclidean distance to both the ideal and anti-ideal solutions. The relative closeness coefficient is computed as the ratio of the distance to the anti-ideal solution over the sum of both distances. The alternative with the highest coefficient is considered the best compromise solution. TOPSIS is particularly suitable for multi-objective optimisation problems because it accounts for both the aspiration to reach ideal performance and the need to stay away from poor solutions, providing a clear, quantitative, and balanced way to select a final solution from a Pareto front.

The methodology employed to objectively determine the weighting of criteria among multiple objectives is based on the entropy weight method, which is grounded in Shannon's information theory [134]. This data-driven approach minimises subjective bias by quantifying the degree of variability or dispersion in each criterion across all considered alternatives [135]. Criteria exhibiting greater variability are interpreted as carrying more informative content and are thus assigned higher weights. In contrast, criteria with minimal variation provide less discriminatory power and are consequently given lower weights. The weights are not fixed but recalculated for each evaluation to reflect the dynamic contribution of each criterion. These adaptive weights are then integrated into the TOPSIS ranking of solutions on the ANN–GA Pareto front, ensuring balanced and context-sensitive optimisation across thermodynamic, economic, and environmental objectives [136,137].

6. Results and discussion

The proposed system is unique in integrating a hybrid PVT-powered ORC using flexible PSC technology, double-effect compression–absorption refrigeration, PEM electrolyser-based hydrogen production, and advanced ANN–GA optimisation, enabling simultaneous multi-carrier generation and comprehensive thermodynamic analysis, which is rarely addressed in existing literature.

6.1. Energy and exergy analysis

A comprehensive exergy analysis is conducted and presented in this section, with the primary objective of identifying and quantifying the major sources of exergy destruction within the overall polygeneration system. This exergetic assessment encompasses all the key components of the system, enabling a deeper understanding of the thermodynamic inefficiencies and the potential for performance improvement. Unlike energy-based assessments, which only track quantity, exergy analysis evaluates quality and the potential of energy to perform useful work—providing a more meaningful basis for system optimisation and design improvements.

A base case scenario is calculated from the data inputs presented in Section 2 for each subsystem. The thermodynamic properties of different states for each subsystem are presented in Table A8. On the other hand, Table 7 outlines critical data regarding system irreversibilities and exergetic performance indicators. These include the fuel and product exergy rates, overall exergy efficiency, exergy destruction rates, destruction ratios, and irreversibility ratios for each subsystem.

It is important to note that, for the base case scenario, the entire energy demand is fully met by solar energy. Consequently, the biomass backup heater is not included in this analysis, as it does not contribute to the system's energy supply under these operating conditions.

As shown in Fig. 8-a, the results reveals that the solar collector subsystem is the predominant source of exergy destruction, accounting for approximately 566.7 kW, which represents 87 % of the total irreversibility of the system. The ORC subsystem is responsible for 44.1 kW (7 %) of the exergy destruction, the cascade refrigeration system contributes to 30.6 kW (5 %), while the PEM electrolyser accounts only for 4 kW (1 %). The total investment cost rate is $ 14.75/h, with the primary contributions distributed as follows: the PTCs represent approximately 57 % of the total cost, the ORC turbine accounts for 19 %, the compressor of the cascaded refrigeration system contributes 7 %, and the PEM electrolyser comprises 2 %.

The Heat Transfer Area (HTA) of the various heat exchangers of the system is shown in Fig. 8-b. Proper sizing of heat exchangers is essential for accurate cost estimation, efficient thermal performance, and overall system optimisation. The heat exchanger for the heating process has the largest HTA at 66 m^2, representing 48.3 % of the total. It is followed by the ORC evaporator, which accounts for 11.2 % (15.6 m^2) of the total HTA. Collectively, the heat exchangers in the cascade refrigeration system make up 36.2 % (48.9 m^2) of the total HTA.

6.2. Parametric analysis

This section presents a parametric analysis of the polygeneration system, where key parameters are varied to evaluate their impact on performance. This approach enhances system understanding, reveals

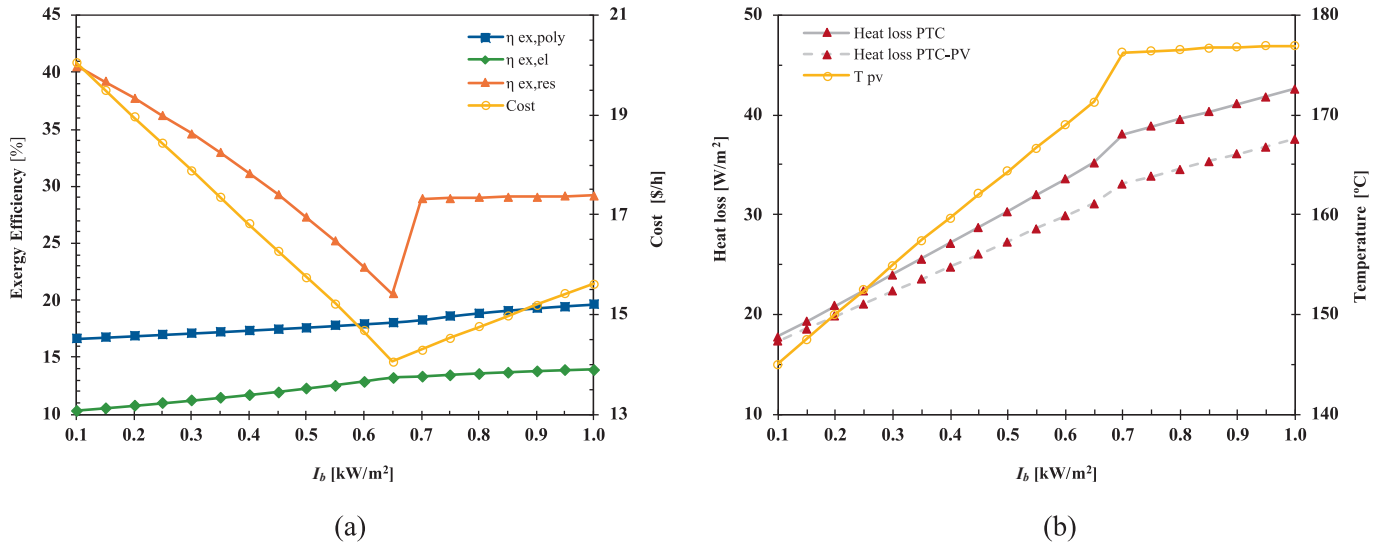

Fig. 10. Effect of DNI on the system efficiency (a) and on the PTCs performance (b).

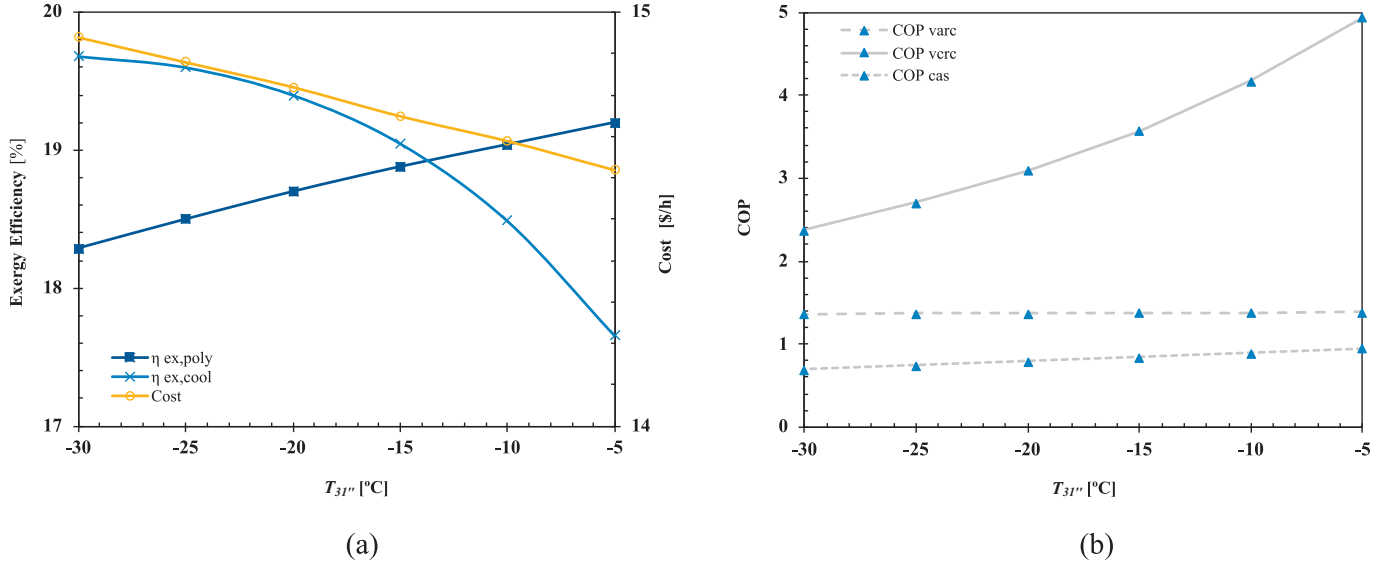

Fig. 11. Effect of evaporation temperature on the system efficiency (a) and on the cooling performance (b).

sensitivities and nonlinearities, and identifies optimal operating ranges. It also supports model validation and informs the selection of input variables for optimisation, ultimately contributing to more robust and efficient system design.

6.2.1. *Effect of ORC evaporator inlet temperature*

The temperature at which heat is supplied to the ORC evaporator significantly influences the system's overall performance, as the optimal evaporation temperature depends directly on the thermal energy provided by the solar field. In this study, as it is illustrated in Fig. 9, we specifically investigate how varying this temperature—from 180 °C to 260 °C—impacts the efficiency of the ORC, the solar sub-subsystem and the overall performance of the polygeneration system.

Increasing the ORC evaporator inlet temperature leads to a rise in both the electrical, solar and polygeneration exergy efficiencies, while simultaneously increasing the cost rate. This improvement is attributed to the efficiency enhancement of the heat recovery within the evaporator. Specifically, when the ORC evaporator inlet temperature increases from 180 °C to 260 °C, the overall exergy efficiency improves by 18 %, reaching a peak value of 21.6 %, while the cost rate increases by 12 %, reaching a maximum value of $16.2/h. On the other hand, as the temperature of the HTF increases, heat losses from both types of solar collectors also rise, as expected. Particular attention must be given to the temperature of the PV cells in the PTC-PV collector. To ensure the structural integrity and long-term performance of the PTC-PV system, continuous operation at PV cell temperatures above 180 °C must be avoided. Based on this analysis, it is therefore concluded that the inlet temperature to the ORC evaporator should remain below 200 °C.

6.2.2. *Effect of solar irradiance*

Although solar radiation is a non-controllable parameter, it varies at different times of the day and in different seasons of the year, which determines the required load of the biomass heater as solar back-up. Fig. 10 represents the effect of Direct Normal Irradiance (I_b) in the range of 0.1–1 kW/m^2 on the system's performance.

The results indicate that both the electrical and polygeneration exergy efficiencies increase as solar irradiance rises from 0.1 to 1 kW/m^2. However, the exergy efficiency of the renewable energy source initially decreases—from 41.8 % to 20.6 %—as solar irradiance increases from 0.1 to 0.65 kW/m^2. Beyond this point, it rises again to

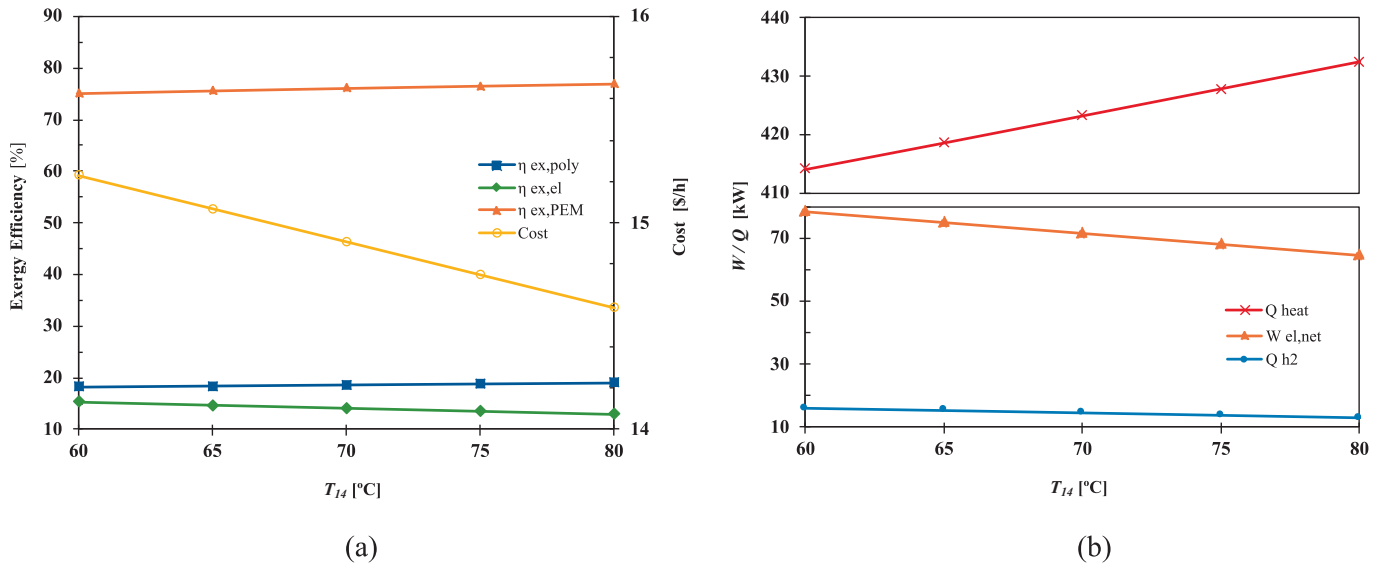

Fig. 12. Effect of the heating temperature on the system efficiency (a) and on the system outputs (b).

Table 8
Optimisation variables.

Parameter	Base case	Examined range
ORC evaporator temperature ($T_{1'}$)	190 °C	[180: 240] °C
Direct Normal Irradiance (I_b)	0.8 kW/m^2	[0: 1] kW/m^2
Evaporation temp. of refrigeration system ($T_{31''}$)	−15 °C	[-5: −30] °C
Temperature of the heating process (T_{14})	75 °C	[60: 80] °C
Condensation temp. of refrigeration system ($T_{20''}$)	25 °C	[15: 30] °C
Power input of PEM electrolyser (Fr_{PEM})	0.25	[0.15: 0.5]

approximately 29 %, remaining relatively stable thereafter. The nonlinear influence of DNI on system performance has important implications for both system sizing and control strategy design. The turning point at 0.65 kW/m^2 indicates a transition between hybrid and fully solar-driven operation, suggesting that key components should be sized to operate efficiently around this threshold rather than at the extremes of irradiance. Oversizing the solar field could lead to unnecessary capital costs and increased thermal losses at high irradiance levels, while undersizing it would increase dependence on the biomass backup system.

Additionally, the system is configured such that when solar energy is the sole input source, the net electrical output ($\dot{W}_{el,net}$) is not capped at 50 kW. As a result, $\dot{W}_{el,ORC}$ increases accordingly and influences the cost curve: during hybrid operation—when both solar and biomass inputs are used—the cost rate decreases from $ 20.6 to 14.1/h as solar irradiance increases from 0.1 to 0.65 kW/m^2. However, beyond 0.65 kW/m^2, when solar becomes the exclusive energy source, the cost begins to rise linearly, reaching a value of $ 15.6/h at 1 kW/m^2.

This phenomenon, as illustrated in Fig. 10-b, also impacts the performance of the solar collectors. As solar irradiance increases, heat losses in the collectors rise linearly. This is primarily due to the simultaneous increase in both the HTF temperature and the absorber tube

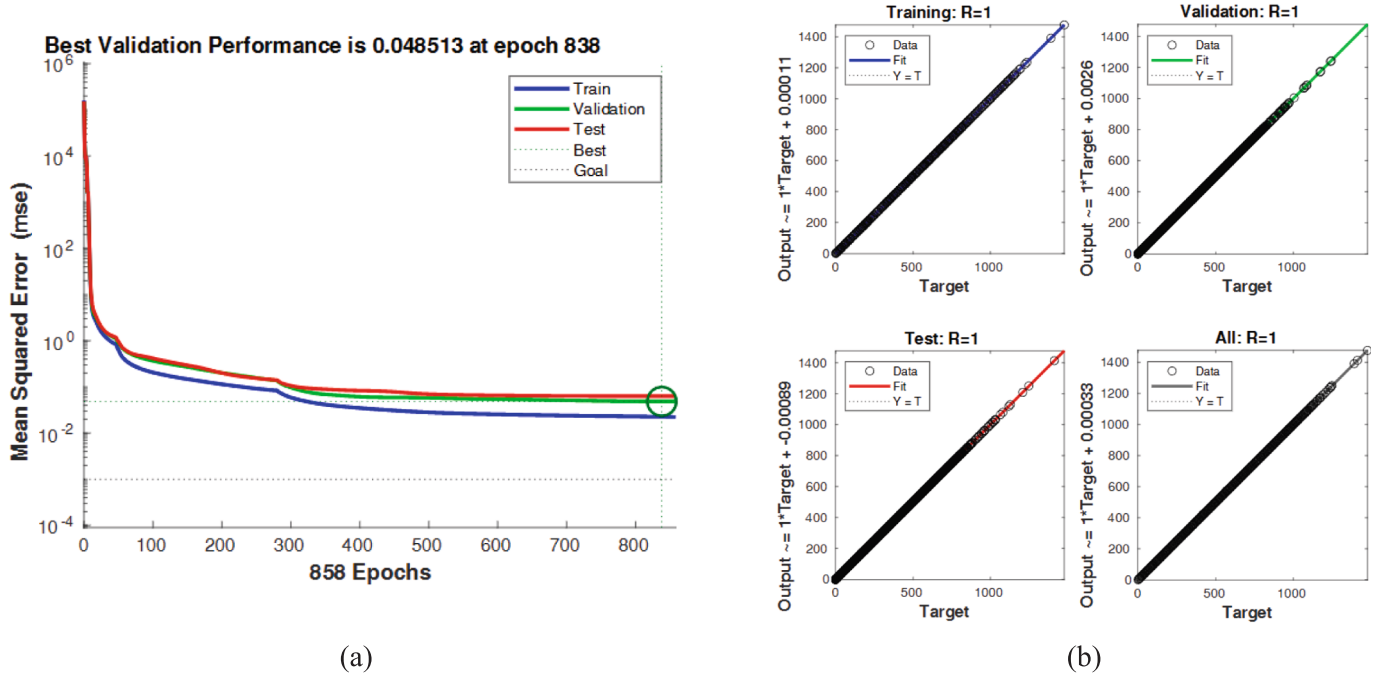

Fig. 13. ANN model: (a) validation performance plot; (b) regression plot (output data vs target).

Table 9
Optimisation results with various optimisation criteria.

Optimisation criteria	Inputs						Outputs					
	T_1 [°C]	I_b [kW/m^2]	$T_{31''}$ [°C]	T_{14} [°C]	$T_{20''}$ [°C]	Fr_{PEM}	$\eta_{ex,poly}$ [%]	$\dot{C}_{tot}$ [$/h]	$\dot{W}_{el,net}$ [kW]	$\dot{Q}_{heat}$ [kW]	$\dot{Q}_{H2}$ [kW]	$\eta_{en,poly}$ [%]	$\dot{E}_{D,tot}$ [kW]
Base case	190.0	0.80	−15.0	75.0	25.0	0.25	18.88	14.75	68.1	427.8	13.7	68.8	649.9
$\eta_{ex,poly}$, $\dot{C}_{tot}$	192.7	0.72	−7.2	79.8	16.4	0.22	19.28	14.16	63.7	384.8	10.3	70.2	583.4
$\eta_{ex,poly}$, $\dot{C}_{tot}$, $\dot{W}_{el,net}$	188.9	0.74	−5.1	76.0	17.0	0.20	19.13	14.25	69.6	401.2	10.3	70.7	604.3

temperature. However, a shift in this trend occurs around 0.65 kW/m^2, where the slope of the heat loss curve begins to flatten as the fluid temperature approaches its maximum target value. A similar pattern is observed in the solar PV cell temperature, which peaks at this inflection point and then remains nearly constant at approximately 177 °C.

6.2.3. *Effect of evaporation temperature of the cascade refrigeration system*

Analysing the effect of the evaporation temperature of the cascaded refrigeration system through a sensitivity analysis is crucial for understanding how variations in this parameter influence both the performance of the subsystem itself and the overall system. As the main application of the analysed cascaded refrigeration system is to produce low-temperature cooling, the evaporation temperature ($T_{31''}$) is examined from −30 to −5 °C. Results are presented in Fig. 11.

Within the analysed temperature range, an inverse relationship is observed between the overall system exergy efficiency and cost, as expected. As the evaporating temperature decreases, the overall exergy efficiency drops at a relative rate of approximately 4 %, while the system cost rate increases at a relative rate of about 2 %. The exergy efficiency of the refrigeration cycle follows a parabolic trend, reaching a maximum of 19.7 % at an evaporating temperature of −30 °C. Meanwhile, the COP of the cascade refrigeration system increases significatively with higher evaporating temperatures, due to the reduced compressor work. The COP_{cas} reaches a maximum value of 0.95 at −5 °C, compared to a minimum of 0.7 observed at −30 °C.

6.2.4. *Effect of heating process temperature*

The temperature of the heating process simultaneously influences two key aspects: (*i*) the condensing temperature of the ORC and (*ii*) the inlet water temperature to the PEM electrolyser. Fig. 12 illustrates the system's performance as a function of the heating temperature, evaluated within the range of 60 °C–80 °C. An increase in this temperature within the analysed range has a positive effect on both the overall exergy efficiency of the system and the exergy efficiency of the PEM electrolyser, while it negatively affects both the ORC electrical efficiency and the cost rate.

The results show that increasing the heating temperature leads to a rise in both the overall exergy efficiency of the system and the exergy efficiency of the PEM electrolyser, by approximately 5 % and 2 %, respectively, over the analysed range. However, the exergy efficiency of the ORC drops notably, from 15.3 % to 13.0 %, due to reduced work output from the turbine as a result of higher condensing temperatures. Consequently, the total cost also decreases by about 4 %, driven by the same reduction in turbine work output.

6.3. *Optimisation results*

From the previous parametric analysis, this section focuses on identifying the system's optimal operating point through a MOO method following the approach explained in Section 5. The optimisation aims to simultaneously maximise overall exergy efficiency and total net power generation while minimising operational costs. This balance of conflicting objectives is essential to achieving a technically and economically viable solution, enabling the system to operate under conditions that provide the best trade-off between performance and cost-effectiveness.

To optimise the entire system using a MOO approach, six key parameters were selected – four of which were previously considered in the parametric analysis, along with two additional ones: the condensation temperature of the cascaded refrigeration system ($T_{20''}$), and the power input of PEM electrolyser (Fr_{PEM}). The operating parameters are varied simultaneously within their specified ranges, as detailed in Table 8.

The ANN model is developed to predict the output responses of the system performance. Fig. 13 shows the model's predictive accuracy in estimating system outputs based on input variables. The observed values of *MSE* and R^2 demonstrate its effectiveness in capturing complex

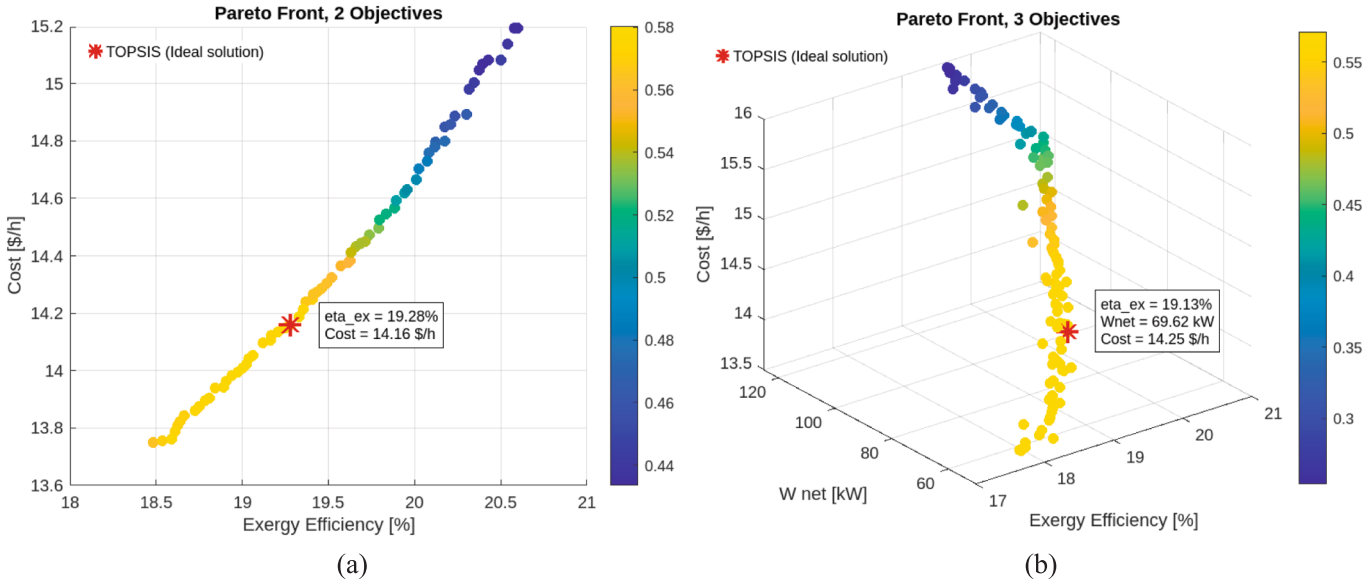

Fig. 14. Pareto front: (a) exergy efficiency vs total cost; (b) exergy efficiency vs net electrical power vs total cost.

Table 10
Optimisation results with various optimisation criteria.

I_b [kW/m^2]	Optimised Inputs					Outputs						
	$T_{1'}$ [°C]	$T_{31''}$ [°C]	T_{14} [°C]	$T_{20''}$ [°C]	Fr_{PEM}	$\eta_{ex,poly}$ [%]	$\dot{C}_{tot}$ [$/h]	$\dot{W}_{el,net}$ [kW]	$\dot{Q}_{heat}$ [kW]	$\dot{Q}_{H2}$ [kW]	$\eta_{en,poly}$ [%]	$\dot{E}_{D,Tot}$ [kW]
0.0	220.6	−5.4	79.4	16.0	0.16	17.97	18.44	50.0	388.5	10.6	94.6	562.5
0.1	216.6	−6.9	79.6	17.5	0.17	18.16	17.82	50.0	382.2	10.7	90.1	560.3
0.2	214.2	−5.2	79.6	15.7	0.20	18.35	17.01	50.0	365.6	11.7	86.2	543.9
0.3	209.2	−7.1	79.3	18.6	0.20	18.35	16.30	50.0	356.4	10.9	81.5	538.9
0.4	206.9	−6.0	79.7	15.1	0.21	18.57	15.34	50.0	333.7	10.6	77.6	514.9
0.5	202.8	−5.6	77.7	15.8	0.23	18.54	14.43	50.0	308.2	10.2	73.2	491.7
0.6	196.5	−5.3	79.8	15.2	0.25	18.71	13.72	50.0	310.7	10.3	70.1	495.4
0.7	188.5	−5.1	79.8	19.0	0.24	18.74	13.91	58.4	379.5	10.0	70.4	572.6
0.8	184.2	−8.2	79.9	16.8	0.20	19.21	14.26	69.9	447.4	10.1	70.7	652.5
0.9	185.8	−9.5	79.9	18.3	0.17	19.70	14.65	84.5	510.1	10.0	70.9	728.6
1.0	182.9	−7.3	79.9	16.3	0.17	19.95	14.84	97.0	581.7	10.8	71.7	808.8

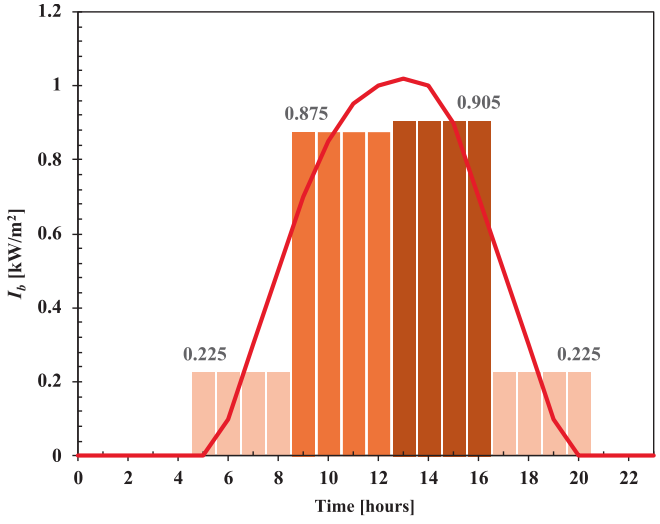

Fig. 15. Solar radiation density variation versus time, Madrid, Spain [138].

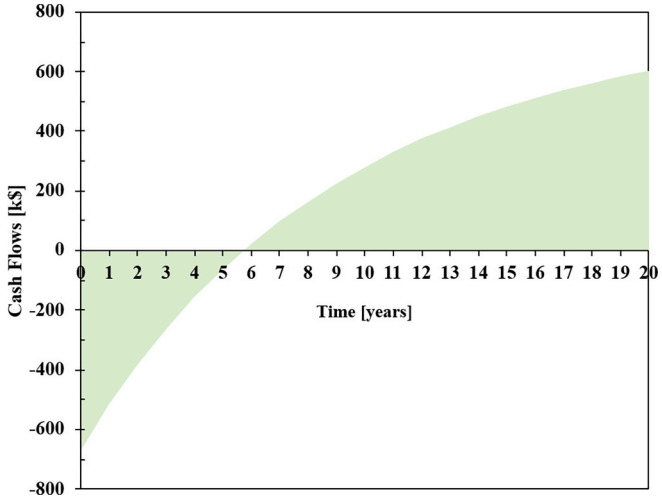

Fig. 16. Cumulative cash flow diagram for the optimised polygeneration system.

nonlinear relationships and supporting reliable optimisation of the polygeneration system.

The three objective functions considered for the integrated system are the total associated cost ($\dot{C}_{tot}$), the system's exergy efficiency ($\eta_{ex,poly}$), and the net electrical power output ($\dot{W}_{el,net}$). As stated, a genetic algorithm-based MOO method is applied to identify the optimal trade-offs among these objectives. Defining the population size and the number of generations is crucial for achieving a well-distributed and converged Pareto front. A larger population increases solution diversity, while more generations allow sufficient exploration and refinement of

Table 11
Financial metrics vs. Energy price variation.

Scenario	Energy price change	Payback (Years)	NPV ($)	IRR (%)
Base	0 %	5.7	602,000 €	11.6 %
High	+10 %	5.3	709,000 €	13.0 %
Very High	+20 %	5.1	815,000 €	14.3 %
Low	−10 %	6.2	496,000 €	10.1 %
Very Low	+20 %	6.7	389,000 €	8.4 %

optimal trade-offs. For the two-objective optimisation, the population size and number of generations are set to 200 and 50, respectively. In the case of the three-objective optimisation, these parameters are increased to 300 and 100 to ensure adequate exploration and convergence of the solution space.

Several constraints were imposed, such as limiting the temperature of the PV cell in the PTC-PV subsystem (T_{PV}) to no more than 180 °C and ensuring a minimum hydrogen production rate ($\dot{Q}_{H_2}$) of 10 kW. The optimal solutions are illustrated in the Pareto front, including the TOPSIS-derived ideal solution. Results are summarised in Table 9 and Fig. 14. An increase in hydrogen production negatively affects the overall system exergy efficiency; therefore, the optimisation algorithm favours minimising hydrogen generation in the PEM electrolyser.

In addition, since solar irradiance is a climatic parameter beyond the control of the plant operator, an optimisation analysis is carried out across the range of solar irradiance values to determine the optimal settings for the remaining five effective parameters within their examined limits. The two objective functions considered are $\dot{C}_{tot}$ and $\eta_{ex,poly}$. The results are presented in Table 10.

For the financial analysis, the revenues of the polygeneration plant depend not only on the unit price of fuels, but also on the operating parameters, which include solar irradiance—a variable that changes throughout the 24-hour day. Madrid (Spain) is selected as the reference location for system operation, and a typical daily profile of direct normal irradiance is estimated (see Fig. 15). The plant is scheduled to operate 16 h per day, from 5:00 a.m. to 8:00 p.m., six days a week, for 52 weeks per year (~5,000 operating hours annually). To maximise financial performance indicators, the day is divided into four irradiance intervals, and the complete system is optimised for each of these intervals.

Fig. 16 illustrates the cash flow diagram for the polygeneration plant, visually depicting the project's financial performance over time. It starts with a significant cash outflow of $667,000 in year 0, representing the initial capital investment. The breakeven point, or payback period, is reached at year 5.7, marking the moment when the project begins to generate net positive cash flows. By year 20, the NPV reaches $602,000, and the IRR is calculated at 11.6 %.

To assess the impact of energy price fluctuations on the economic performance of the proposed system, a sensitivity analysis is conducted considering both increases and decreases in energy prices starting from year 3 of operation (see Table 11). The investment cost and interest rate are kept fixed, as these inputs are treated as predetermined parameters in the financial model.

The analysis evaluates the resulting changes in NPV, payback period, and IRR, providing insight into the robustness of the system's economic performance under realistic variations in energy market conditions. The results demonstrate a positive return on investment and solid economic performance over its operational lifetime.

7. Conclusions

This study presents the design, modelling, and optimisation of a novel ORC-based polygeneration system entirely powered by renewable energy sources. The configuration uniquely integrates a hybrid PVT-powered ORC, a double-effect compression–absorption refrigeration system, and hydrogen production via a PEM electrolyser. These innovations enable simultaneous multi-carrier generation, comprehensive thermodynamic evaluation, and intelligent optimisation, demonstrating the system's strong potential for efficient and sustainable energy conversion compared with conventional configurations.

Integrating cascade subsystems that utilise residual heat significantly enhances the overall energy utilisation of the polygeneration system. This cascading approach effectively harnesses low-grade thermal energy from upstream processes, promotes synergistic operation among components, enables simultaneous multi-carrier generation, and improves overall exergy efficiency. The results demonstrate the system's strong technical and economic viability, positioning it as a promising zero-emissions solution for integrated energy generation and storage. The financial analysis reveals that, over a 20-year period, the project achieves a PBP of 5.7 years, a NPV of $602,000, and an IRR of 11.6 %. Its applications are particularly relevant for both buildings (e.g., offices, hospitals, and university campuses) and energy-intensive industries (e.g., food and beverage, chemical, plastics manufacturing, and metallurgical sectors).

The novel hybrid optimisation framework combining an ANN with a multi-objective genetic algorithm proved effective for exploring the performance–cost trade-offs of the proposed system. The ANN enabled rapid and accurate prediction of thermodynamic responses, substantially reducing computational time compared to direct thermodynamic simulations. This approach efficiently identified Pareto-optimal solutions balancing exergy efficiency and cost rate. The results demonstrate that hybrid data-driven optimisation is a powerful tool for complex energy systems, providing valuable insights into design flexibility and enabling decision-makers to select optimal configurations.

Steady-state modelling allows for detailed energy and exergy analysis, as well as validation of subsystem models, without the additional complexity and computational cost of dynamic simulations. Nevertheless, transient variations in solar irradiance, load demand, or ambient conditions may affect system performance. Therefore, future work will incorporate long-term dynamic simulations, detailed loss modelling, and evaluations of scalability and techno-economic feasibility to better capture the system's behaviour under realistic, time-varying operating conditions and to complement the insights obtained from the steady-state analysis.

Although the integration of perovskite photovoltaic technology within the hybrid PVT collector enables high theoretical electrical and thermal efficiencies and compact design, the long-term stability of perovskite materials under real operating conditions (moderate operating temperatures < 200 °C) remains a major challenge for large-scale deployment. The proposed PVT configuration demonstrates strong thermodynamic potential, but its feasibility in real engineering applications will depend on future progress in material stabilisation and module packaging technologies.

The high exergy destruction in the solar subsystem (87 %) primarily reflects optical and thermal losses inherent to the hybrid PVT concentrator; however, it also indicates that the remaining subsystems are well-sized and thermodynamically optimized, minimizing internal irreversibilities. Future work will aim to reduce solar exergy losses through advanced selective coatings, improved concentrator and receiver geometries, and enhanced thermal management designs to further increase overall system efficiency.

CRediT authorship contribution statement

Jesús García-Domínguez: Writing – review & editing, Writing – original draft, Visualization, Software, Methodology, Investigation, Formal analysis, Data curation, Conceptualization. **J. Daniel Marcos:** Writing – review & editing, Validation, Resources, Funding acquisition, Methodology, Formal analysis, Conceptualization. **Ana M. Blanco-Marigorta:** Writing – review & editing, Validation, Software, Methodology, Formal analysis, Conceptualization. **Pablo A. García-Salaberri:** Writing – review & editing, Validation, Formal analysis.

Declaration of competing interest

The authors declare that they have no known competing financial interests or personal relationships that could have appeared to influence the work reported in this paper.

Acknowledgement

This work received no direct financial support; however, the authors gratefully acknowledge the support provided by the Comunidad de Madrid through the ACES4NET0-CM project and by the Spanish Research Council through the project TED2021-131620B-C21.

Appendix

Table A1
ORC working fluids [65,68,69].

Fluid	Boiling point (°C)	Critical temperature (°C)	Critical pressure (MPa)	Thermal stability limit (°C)	Environmental impact (GWP / ODP)	Comments
Toluene	110.6	318.6	4.11	~400	Low / 0	High-temperature stability, high efficiency, low GWP
n-Pentane	36.1	196.6	3.37	~250	Low / 0	Good efficiency, but limited by lower temperature range
Cyclohexane	80.7	280.5	4.07	~350	Low / 0	Good stability, but higher flammability risk
Benzene	80.1	288.9	4.89	~380	Low / 0 (toxic)	Excellent thermodynamic efficiency, but toxic
MDM	~152	~290	1.44	~350	Very low / 0	Stable and safe, but less efficient at high temperature
R245fa	15.3	154.0	3.65	~200	~950 / 0	Suitable for low-temperature ORC, higher GWP

Table A2
Therminol 66 Property Data [89].

Fluid parameter	Properties
Service Temperature	−3 to 345 °C
Density	1020–770 kg/m^3
Specific Heat	1.49–2.78 kJ/kg-K
Thermal Conductivity	0.118–0.089 W/m-K
Dynamic Viscosity	2.92 @110 °C / 0.5 @270 °C mPa-s
Vapor Pressure	0.2 @ 280 °C atm

Table A3
Definition of dead-state pressures for each subsystem.

Subsystem	Dead-state pressure	Determination criterion	Reference / justification
Solar field	$P_{0,sol} = 150$ kPa	Intermediate value between HTF operating pressure and atmospheric pressure	Consistent with methodology in [60]
ORC	$P_{0,ORC} = 3.8$ kPa	Saturation pressure of toluene at $T_0 = 25$ °C	EES built-in property data
VCRC	$P_{0,VCRC} = 68.9$ kPa	Saturation pressure of n-pentane at $T_0 = 25$ °C	EES built-in property data
VARC	$P_{0,VARC} = 1.2$ kPa	Equal to absorber outlet pressure; LiBr concentration $X_{0,LiBr}$ at chemical equilibrium (44 %)	EES built-in property data based on Patek–Klomfar correlation
PEM electrolyser	$P_{0,PEM} = 101.3$ kPa	Atmospheric pressure (nominal operating condition)	Standard reference environment

Table A4
Exergy balance for each subsystem.

Subsystem	Balance	Exergy efficiency
Solar field + biomass backup heater	$\dot{E}_{F,res} = \dot{E}x_{in}$ $\dot{E}_{P,res} = \left(\dot{E}x_{1'} - \dot{E}x_{5'}\right) + \dot{W}_{el,PV}$	$\eta_{ex,res} = \frac{\dot{E}_{P,res}}{\dot{E}_{F,res}}$
ORC	$\dot{E}_{F,ORC} = \left(\dot{E}x_{1'} - \dot{E}x_{4'}\right) + \dot{W}_{ORC,pump}$ $\dot{E}_{P,ORC} = \dot{W}_{el,ORC} + \left(\dot{E}x_{14} - \dot{E}x_{13}\right) + \left(\dot{E}x_{2''} - \dot{E}x_{1''}\right)$	$\eta_{ex,ORC} = \frac{\dot{E}_{P,ORC}}{\dot{E}_{F,ORC}}$

(continued on next page)

Table A4 (*continued*)

Subsystem	Balance	Exergy efficiency
Cascaded refrigeration	$\dot{E}_{F,cool} = \left(\dot{E}x_{4'} - \dot{E}x_{5'}\right) + \dot{W}_{el,co} + \dot{W}_{S,pump}$ $\dot{E}_{P,cool} = \dot{E}x_{30''} - \dot{E}x_{31''}$ $\dot{E}_{L,cool} = \left(\dot{E}x_{21''} - \dot{E}x_{20''}\right) + \left(\dot{E}x_{23''} - \dot{E}x_{22''}\right)$	$\eta_{ex,cool} = \frac{\dot{E}_{P,cool}}{\dot{E}_{F,cool}}$
PEM electrolyser	$\dot{E}_{F,PEM} = \dot{W}_{el,PEM} + (\dot{E}x_{11} - \dot{E}x_{12})$ $\dot{E}_{P,PEM} = \dot{E}x_{5''} + \dot{E}x_{6''}$	$\eta_{ex,PEM} = \frac{\dot{E}_{P,PEM}}{\dot{E}_{F,PEM}}$

The fuel–product formulation is not directly applicable to dissipative components such as expansion valves of the cascaded refrigeration system. Therefore, the approach adopted in this study is to treat the valves as components serving the corresponding downstream heat exchanger [118].

Table A5
Investment cost function of components [58,119–122].

Component	Cost function (Z_k [$])
PTC-PV	$Z_{PTC-PV} = 240\left(A_{ap,PTC-PV}\right)^{0.71} + 1500\left(\dot{W}_{el,PV}\right)$
PTC	$Z_{PTC-PV} = 240\left(A_{ap,PTC}\right)^{0.71}$
Storage tank	$Z_t = 575621\left(\frac{V_t}{3000}\right)^{0.8}$
Biomass backup heater	$Z_{bh} = 255\left(\dot{Q}_{bh}\right)$
ORC Turbine	$Z_{ORC} = 4750\left(\dot{W}_{el,ORC}\right)^{0.75}$
Regenerator	$Z_{reg} = 1173\left(\dot{m}_{ORC}\right)$
Pumps	$Z_{pump,k} = 3750\left(\dot{W}_{pump,k}\right)^{0.71}$
High desorber	$Z_{hd} = 17500\left(\frac{A_{hd}}{100}\right)^{0.6}$
High condenser – Low desorber	$Z_{hc-ld} = 16000\left(\frac{A_{hc-ld}}{100}\right)^{0.6}$
Low condenser	$Z_{cond} = 8000\left(\frac{A_{cond}}{100}\right)^{0.6}$
Absorber	$Z_{abs} = 16000\left(\frac{A_{abs}}{100}\right)^{0.6}$
Compressor	$Z_{co} = 10167.5\left(\dot{W}_{el,co}\right)^{0.46}$
Evaporator	$Z_{eva} = 1397\left(A_{eva}\right)^{0.89}$
PEM Electrolyser	$Z_{PEM} = 800\left(\dot{W}_{el,PEM}\right)$
Heat exchangers	$Z_{HX,k} = 2143\left(A_{HX,k}\right)^{0.514}$
Expansion valves	$Z_{val} = 500$

Table A6
Overall heat transfer coefficient for the heat exchangers [55,90,120].

Heat exchanger	U[kW/m^{2}K]
ORC Evaporator (SH, EVA, ECO)	1.275
High desorber	1.5
High condenser – Low desorber	0.55
Low condenser	2.5
Cascade HX	0.55
Absorber	0.7
Solution HX 1, HX 2	1.0
Evaporator	1.5
Rest of Heat Exchangers	0.55

Table A7
Price of fuels for the energy streams [123–125].

Fuel	Price
Electricity	0.16 $/kWh
Cooling[a]	0.095 $/kWh
Heating	0.055 $/kWh
Hydrogen	6.9 $/kg
Biomass	0.08 $/kg

[a]The price for cooling is estimated for a 85 kW vapor compression chiller with a COP of 1.8 and a total CAPEX of $ 80,000, using the financial parameters outlined in Section 3.3.
[b]The price for heating is estimated based on a 450 kW gas-fired boiler with 90 % thermal efficiency and a total CAPEX of $ 112,000, using the financial assumptions detailed in Section 3.3 and applying natural gas prices relevant to non-household consumers in Spain.

Table A8
Thermodynamic properties of the streams (base case).

Subsystem	State no.	Fluid	$\dot{m}$[kg/s]	T[°C]	P[kPa]	h[kJ/kg]	s[kJ/kgK]	$\dot{E}x^{ph}$[kW]	$\dot{E}x^{ch}$[kW]	$\dot{E}x$[kW]
Solar	1′	Therminol-66	7.84	190.0	300	356.9	0.986	516.9		516.9
	2′	Therminol-66	7.84	188.7	300	354.1	0.979	509.2		509.2
	3′	Therminol-66	7.84	163.0	300	299.3	0.858	361.8		361.8
	4′	Therminol-66	7.84	160.3	300	293.5	0.845	346.2		346.2
	5′	Therminol-66	7.84	155.3	300	283.7	0.822	324.3		324.3
	6′	Therminol-66	7.84	164.1	300	302.0	0.863	371.7		371.7
	7′	Therminol-66	3.92	173.8	300	322.3	0.904	423.1		423.1
	8′	Therminol-66	7.84	198.5	300	375.2	1.024	568.7		568.7
	9′	Therminol-66	6.27	187.9	300	352.3	0.975	403.3		403.3
	10′	Therminol-66	6.27	166.3	300	306.6	0.874	306.5		306.5
	11′	Therminol-66	7.84	190.0	300	356.9	0.986	516.9		516.9
ORC	1	Toluene	1.12	83.0	43.4	−53.9	−0.145	10.2		10.2
	2	Toluene	1.12	83.1	185.1	−53.6	−0.145	10.4		10.4
	3	Toluene	1.12	109.9	185.1	−1.3	−0.004	21.8		21.8
	4	Toluene	1.26	133.1	185.1	46.1	0.116	39.2		39.2
	5	Toluene	1.26	133.2	308.5	46.3	0.117	39.4		39.4
	6	Toluene	1.26	150.0	308.5	82.1	0.203	52.1		52.1
	7	Toluene	1.26	155.0	308.5	421.8	0.996	182.6		182.6
	8	Toluene	1.26	165.0	308.5	439.3	1.037	189.5		189.5
	9	Toluene	0.14	152.8	185.1	423.5	1.043	18.6		18.6
	10	Toluene	1.12	121.4	43.4	379.8	1.064	92.5		92.5
	11	Toluene	1.12	85.2	43.4	327.4	0.925	80.3		80.3
	12	Toluene	1.12	84.0	43.4	325.7	0.919	79.9		79.9
	13	Water	15.0	68.2		285.4	0.933	180.9		180.9
	14	Water	15.0	75.0		314.0	1.015	239.0		239.0
Cascaded refrigeration	1″	Water-LiBr	0.40	36.1	1.23	80.3	0.243	0.17	3.32	3.50
	2″	Water-LiBr	0.40	36.2	6.90	80.3	0.243	0.17	3.32	3.50

(continued on next page)

Table A8 (*continued*)

Subsystem	State no.	Fluid	$\dot{m}$[kg/s]	T[°C]	P[kPa]	h[kJ/kg]	s[kJ/kgK]	$\dot{E}x^{ph}$[kW]	$\dot{E}x^{ch}$[kW]	$\dot{E}x$[kW]
	3″	Water-LiBr	0.40	62.5	6.90	135.9	0.414	1.85	3.32	5.17
	4″	Water-LiBr	0.36	82.6	6.90	197.8	0.476	3.41	10.11	13.52
	5″	Water-LiBr	0.36	50.1	6.90	135.2	0.291	0.69	10.11	10.80
	6″	Water-LiBr	0.36	49.2	1.23	135.2	0.285	0.64	10.11	10.75
	7″	Water	0.02	68.6	6.90	2627.7	8.452	4.83		4.83
	8″	Water	0.04	38.7	6.90	162.3	0.555	5.89		5.89
	9″	Water	0.04	10.0	1.23	162.3	0.576	5.61		5.61
	10″	Water	0.04	10.0	1.23	2518.9	8.899	0.03		0.03
	11″	Water-LiBr	0.22	68.6	6.90	148.8	0.452	1.38	1.86	3.24
	12″	Water-LiBr	0.22	68.6	59.11	148.8	0.452	1.38	1.86	3.24
	13″	Water-LiBr	0.22	107.3	59.11	231.0	0.683	4.62	1.86	6.48
	14″	Water-LiBr	0.20	137.0	59.11	303.1	0.756	6.62	5.65	12.27
	15″	Water-LiBr	0.20	89.1	59.11	210.5	0.512	2.34	5.65	7.99
	16″	Water-LiBr	0.20	83.1	6.90	210.5	0.479	1.94	5.65	7.59
	17″	Water	0.02	121.4	59.11	2723.1	7.724	14.01		14.01
	18″	Water	0.02	85.6	59.11	358.3	1.141	3.84		3.84
	19″	Water	0.02	38.7	6.90	358.3	1.184	3.51		3.51
	20″	Water	5.00	25.0		104.8	0.367	0.00		0.00
	21″	Water	5.00	31.2		130.6	0.453	1.39		1.39
	22″	Water	5.00	31.2		130.6	0.453	1.39		1.39
	23″	Water	5.00	33.7		141.4	0.488	2.74		2.74
	24″	n-pentane	0.24	4.5	6.84	334.6	1.381	−1.42		−1.42
	25″	n-pentane	0.24	59.2	57.08	425.3	1.437	20.00		20.00
	26″	n-pentane	0.24	15.0	57.08	−25.1	−0.084	16.79		16.79
	27″	n-pentane	0.24	−1.8	57.08	−62.7	−0.218	17.37		17.37
	28″	n-pentane	0.24	−25.0	6.84	−62.7	−0.209	16.72		16.72
	29″	n-pentane	0.24	−20.0	6.84	297.0	1.239	−0.33		−0.33
	30″	Water-glycol	3.00	−7.1		−47.8	−0.413	343.5		343.5
	31″	Water-glycol	3.00	−15.0		−76.2	−0.518	352.2		352.2
Hydrogen	1‴	Water	$1.0x10^{-3}$	25.0	101.3	104.8	0.367	0.00		0.00
	2‴	Water	$1.0x10^{-3}$	80.0	101.3	335.0	1.075	0.07		0.07
	3‴	Water	$1.3x10^{-3}$	80.0	101.3	335.0	1.075	0.07		0.07
	4‴	Water	$1.3x10^{-3}$	80.0	101.3	335.0	1.075	0.07		0.07
	5‴	Hydrogen	$1.1x10^{-4}$	80.0	101.3	4723	55.81	0.01	13.34	13.35
	6‴	Oxygen	$0.9x10^{-3}$	80.0	101.3	50.5	0.15	0.01	0.11	0.12

Data availability

Data will be made available on request.

References

[1] Wieland C, Schifflechner C, Dawo F, Astolf M. The organic Rankine cycle power systems market: recent developments and future perspectives. Appl Therm Eng 2023;224:119980.

[2] Tchanche BF, Lambrinos G, Frangoudakis A, Papadakis G. Low-grade heat conversion into power using organic Rankine cycles – a review of various applications. Renew Sustain Energy Rev 2011;15:3963–79.

[3] Branchini L, De Pascale A, Peretto A. Systematic comparison of ORC configurations by means of comprehensive performance indexes. Appl Therm Eng 2013;61:129–40.

[4] García-Domínguez J, Marcos JD. Thermodynamic analysis and systematic comparison of solar-heated trigeneration systems based on ORC and absorption heat pump. Energies 2021;14:4770.

[5] Javed S, Tiwari AK. Performance assessment of different Organic Rankine Cycle (ORC) configurations driven by solar energy. Process Saf Environ Prot 2023;171:655–66.

[6] Rayegan R, Tao YX. A procedure to select working fluids for solar Organic Rankine Cycles (ORCs). Renew Energy 2011;36:659–70.

[7] Long R, Bao YJ, Huang XM, Liu W. Exergy analysis and working fluid selection of organic Rankine cycle for low grade waste heat recovery. Energy 2014;73:475–83.

[8] Arjunan P, Gnana Muthu JH, Somanasari Radha SL, Suryan A. Selection of working fluids for solar organic Rankine cycle-a review. Int J Energy Res 2022;46:20573–99.

[9] Nguyen VN, Pham NDK, Duong XQ, et al. Combination of solar with organic Rankine cycle as a potential solution for clean energy production. Sustainable Energy Technol Assess 2023;57:103161.

[10] Loni R, Mahian O, Markides CN, Bellos E, Le Roux WG, et al. A review of solar-driven organic Rankine cycles: recent challenges and future outlook. Renew Sustain Energy Rev 2021;150:111410.

[11] Mortadi M, El Fadar A, Achkari OB. Concentrating and non-concentrating photovoltaic thermal collectors: technologies, applications, exhaustive assessment and challenges. Sol Energy Mater Sol Cells 2024;271:112858.

[12] Herez A, El Hage H, Lemenand T, Ramadan M, Khaled M. Review on photovoltaic/thermal hybrid solar collectors: classifications, applications and new systems. Sol Energy 2020;207:1321–47.

[13] Jacob J, Pandey AK, Rahim NA, Selvaraj J, Samykano M, Saidur R, et al. Concentrated photovoltaic thermal (CPVT) systems: recent advancements in clean energy applications, thermal management and storage. J Storage Mater 2022;45:103369.

[14] Daneshazarian R, Cuce E, Cuce PM, Sher F. Concentrating photovoltaic thermal (CPVT) collectors and systems: theory, performance assessment and applications. Renew Sustain Energy Rev 2018;81(1):473–92.

[15] Ju X, Xu C, Liao Z, Du X, Wei G, Wang Z, et al. A review of concentrated photovoltaic-thermal (CPVT) hybrid solar systems with waste heat recovery (WHR). Sci Bulletin 2017;62:20.

[16] Mortadi M, El Fadar A. Novel design of concentrating photovoltaic thermal collector – a comparative analysis with existing configurations. Energ Conver Manage 2022;268:116016.

[17] Wu J, Zhang X, Shen J, et al. A review of thermal absorbers and their integration methods for the combined solar photovoltaic/thermal (PV/T) modules. Renew Sustain Energy Rev 2017;75:839–54.

[18] S. Wijewardane, L.L. Kazmerski, Inventions, innovations, and new technologies: Flexible and lightweight thin-film solar PV based on CIGS, CdTe, and a-Si:H, Solar Compass 2023, 7, 100053. https://www.sciencedirect.com/science/article/pii/S2772940023000218.

[19] Popoola IK, Gondal MA, Qahtan TF. Recent progress in flexible perovskite solar cells: materials, mechanical tolerance and stability. Renew Sustain Energy Rev 2018;82(3):3127–51.

[20] R. Jani, K. Bhargava, Perovskite-Based Flexible Solar Cells from: Smart and Flexible Energy Devices 2022, CRC Press. https://www.taylorfrancis.com/chapters/edit/10.1201/9781003186755-15/perovskite-based-flexible-solar-cells-rushi-jani-kshitij-bhargava.

[21] Kim HS, Lee CR, Im JH, et al. Lead iodide perovskite sensitized all-solid-state submicron thin film mesoscopic solar cell with efficiency exceeding 9%. Sci Rep 2012;2:591.

[22] Aftab S, Hussain S, Kabir F, Aslam M, Rajpar AH, Al-Sehemi AG. Advances in flexible perovskite solar cells: a comprehensive review. Nano Energy 2024;120:109112.

[23] Kumar P, Shankar G, Kumar A, Najar A, Pradhan B. Recent progress in all-perovskite tandem solar cells and modules: redefining limits. Prog Mater Sci 2026;156:101560.
[24] National Renewable Energy Laboratory, Best Research-Cell Efficiency Chart https://www.nrel.gov/pv/cell-efficiency.html (Accessed on 30 June 2025).
[25] Huang G, Arya PH, Ritzer DB, et al. Hybrid perovskite-photovoltaic and solar-thermal harvesting. Adv Sci 2025. e09692.
[26] Mokabane PT, Lukong VT, Jen TC. A review of the effect of stability issues and wide-bandgap in the application of perovskite solar cells. Mater Renew Sustain Energy 2025;14:34.
[27] Zhang H, Luo Y, Dela Peña TA, Ma R, et al. Latest strategies promoting stable and efficient perovskite, organic, and perovskite-organic tandem solar cells. Adv Mater Interf 2025;12:2500204.
[28] Lykas P, Georgousis N, Bellos E, Tzivanidis C. A comprehensive review of solar-driven multigeneration systems with hydrogen production. Int J Hydrogen Energy 2023;48(2):437–77.
[29] Kasaeian A, Bellos E, Shamaeizadeh A, Tzivanidis C. Solar-driven polygeneration systems: recent progress and outlook. Appl Energy 2020;264:114764.
[30] Gallandat N, Romanowicz K, Züttel A. An analytical model for the electrolyser performance derived from materials parameters. J Power Energy Eng 2017;5:10.
[31] Schalenbach M, Zeradjanin AR, Kasian O, Cherevko S, Mayrhofer KJ. A perspective on low-temperature water electrolysis – challenges in alkaline and acidic technology. Int J Electrochem Sci 2018;13(2):1173–226.
[32] Mucci S, Mitsos A, Bongartz D. Power-to-X processes based on PEM water electrolyzers: a review of process integration and flexible operation. Comput Chem Eng 2023;175:108260.
[33] Rahim AA, Tijani AS, Kamarudin SK, Hanapi S. An overview of polymer electrolyte membrane electrolyzer for hydrogen production: Modeling and mass transport. J Power Sources 2016;309:56–65.
[34] Noor Azam AMI, Li NK, Zulkefli NN, et al. Parametric study and electrocatalyst of polymer electrolyte membrane (PEM) electrolysis performance. Polymers 2023;15(3):560.
[35] García-Salaberri PA, van Eijk L, Bangay W, Ferner KJ, et al. Materials engineering for high performance and durability proton exchange membrane water electrolyzers. ACS Appl Energy Mater 2025;8(18):13050–121.
[36] Karabuga A, Utlu Z, Yakut MZ. Exergy and economic approaches for integrating power and green hydrogen production with a novel solar-ORC system. Therm Sci Eng Prog 2025;61:103552.
[37] Shabani MJ, Babaelahi M. Innovative solar-based multi-generation system for sustainable power generation, desalination, hydrogen production, and refrigeration in a novel configuration. Int J Hydrogen Energy 2024;59:1115–31.
[38] Fouda A, Khaliq A, Elattar HF, Al-Zahrani A, Almohammadi BA, Refaey HA. Evaluation of a concentrated solar power-driven system designed for combined production of cooling and hydrogen. Case Stud Therm Eng 2024;59:104567.
[39] Qing X. Solar-driven multi-generation system: thermoeconomic and environmental optimization for power, cooling, and liquefied hydrogen production. Energy 2024;293:130409.
[40] Yuksel YE, Ozturk M, Dincer I. Design and analysis of a new solar hydrogen plant for power, methane, ammonia and urea generation. Int J Hydrogen Energy 2022;47(45):19422–45.
[41] Raja AA, Huang Y. Novel parabolic trough solar collector and solar photovoltaic/thermal hybrid system for multi-generational systems. Energ Conver Manage 2020;211.
[42] Saeed MZ, Contiero L, Blust S, Allouche Y, Hafner A, Eikevik TM. Ultra-low-temperature refrigeration systems: a review and performance comparison of refrigerants and configurations. Energies 2023;16(21):7274.
[43] Fernández-Seara J, Sieres J, Vázquez M. Compression–absorption cascade refrigeration system. Appl Therm Eng 2006;26(5–6):502–12.
[44] Cimsit C, Ozturk IT. Analysis of compression–absorption cascade refrigeration cycles. Appl Therm Eng 2012;40:311–7.
[45] Jain V, Kachhwaha SS, Sachdeva G. Thermodynamic performance analysis of a vapor compression–absorption cascaded refrigeration system. Energ Conver Manage 2013;75:685–700.
[46] Cimsit C, Ozturk IT, Kincay O. Thermoeconomic optimization of LiBr/H_2O-R134a compression-absorption cascade refrigeration cycle. Appl Therm Eng 2015;76:105–15.
[47] Patel B, Desai NB, Kachhwaha SS. Optimization of waste heat based organic Rankine cycle powered cascaded vapor compression-absorption refrigeration system. Energ Conver Manage 2017;154:576–90.
[48] Jain V, Sachdeva G, Kachhwaha SS. Comparative performance study and advanced exergy analysis of novel vapor compression-absorption integrated refrigeration system. Energ Conver Manage 2018;172:81–97.
[49] Herrera-Romero JV, Colorado-Garrido D. Comparative study of a compression–absorption cascade system operating with NH_3-$LiNO_3$, NH_3-NaSCN, NH_3-H_2O, and R134a as working fluids. Processes 2020;8(7):816.
[50] Zhang H, Pan X, Chen J, Xie J. Energy, exergy, economic and environmental analyses of a cascade absorption-compression refrigeration system using two-stage compression with complete intercooling. Appl Therm Eng 2023;225:120185.
[51] Du Y, Chi C, Wang X. Energy, exergy, and economic analysis of compression-absorption cascade refrigeration cycle using different working fluids. Energy Storage Sav 2024;3(2):87–95.
[52] Colorado D, Rivera W. Performance comparison between a conventional vapor compression and compression-absorption single-stage and double-stage systems used for refrigeration. Appl Therm Eng 2015;87:273–85.
[53] Dixit M, Arora A, Kaushik SC. Energy, exergy, environment and economic analyses and optimization of two-stage absorption–compression combined refrigeration system. Clean Techn Environ Policy 2017;19:2215–29.
[54] Cimsit C. Thermodynamic performance analysis of the double effect absorption-vapor compression cascade refrigeration cycle. J Therm Sci Technol 2018;13(1):JTST0007.
[55] Mussati SF, Morosuk T, Mussati MC. Superstructure-based optimization of vapor compression-absorption cascade refrigeration systems. Entropy 2020;22(4):428.
[56] Izadi A, Shahafve M, Ahmadi P. Neural network genetic algorithm optimization of a transient hybrid renewable energy system with solar/wind and hydrogen storage system for zero energy buildings at various climate conditions. Energ Conver Manage 2022;260:115593.
[57] O. Rejeb, S.M. Alirahmi, E. Assareh, et al., Innovative integrated solar powered polygeneration system for green Hydrogen, Oxygen, electricity and heat production, Energy Conversion and Management 2022, 269, 116073. https://www.sciencedirect.com/science/article/abs/pii/S0196890422008603.
[58] Hai T, Asadollahzadeh M, Chauhan BS, et al. Machine learning optimization and 4E analysis of a CCHP system integrated into a greenhouse system for carbon dioxide capturing. Energy 2024;309:133028.
[59] Alirahmi SM, Assareh E, Arabkoohsar A, et al. Development and multi-criteria optimization of a solar thermal power plant integrated with PEM electrolyzer and thermoelectric generator. Int J Hydrogen Energy 2022;47(57):23919–34.
[60] García-Domínguez J, Blanco-Marigorta AM, Marcos JD. Analysis of a solar driven ORC-absorption based CCHP system from a novel exergy approach. Energy Convers Manage: X 2023;19:100402.
[61] Zhang X, Zhang C, He M, Wang J. Selection and evaluation of dry and isentropic organic working fluids used in organic rankine cycle based on the turning point on their saturated vapor curves. J Therm Sci 2019;28:643–58.
[62] Song C, Gu M, Miao Z, Liu C, Xu J. Effect of fluid dryness and critical temperature on trans-critical organic Rankine cycle. Energy 2019;174:97–109.
[63] Bellos E, Tzivanidis C. Parametric analysis and optimization of a solar driven trigeneration system based on ORC and absorption heat pump. J Clean Prod 2017;16110:493–509.
[64] Yu H, Helland H, Yu X, Gundersen T, Sin G. Optimal design and operation of an Organic Rankine Cycle (ORC) system driven by solar energy with sensible thermal energy storage. Energ Conver Manage 2021;244:114494.
[65] Jafary S, Khalilarya S, Shawabkeh A, Wae-hayee M, Hashemian M. A complete energetic and exergetic analysis of a solar powered trigeneration system with two novel organic Rankine cycle (ORC) configurations. J Clean Prod 2021;281:124552.
[66] Al-Sulaiman FA, Dincer I, Hamdullahpur F. Exergy modeling of a new solar driven trigeneration system. Sol Energy 2011;85(9):2228–22243.
[67] Tzivanidis C, Bellos E, Antonopoulos KA. Energetic and financial investigation of a stand-alone solar-thermal Organic Rankine Cycle power plant. Energ Conver Manage 2016;126:421–33.
[68] Lemmon EW, Span R. Short fundamental equations of state for 20 industrial fluids. J Chem Eng Data 2006;51(3):785–850.
[69] https://pubchem.ncbi.nlm.nih.gov/ (Accessed 12 October 2025).
[70] Dupré O, Vaillon R, Green MA. Physics of the temperature coefficients of solar cells. Sol Energy Mater Sol Cells 2015;140:92–100.
[71] Moot T, Patel JB, McAndrews G, et al. Temperature coefficients of perovskite photovoltaics for energy yield calculations. ACS Energy Lett 2021;6(5):2038–47.
[72] Yan G, Zhou X, Abed AM, Alsenani TR, Elattar S, Peng F, et al. Proposing and optimization of a parabolic trough solar collector integrated with a photovoltaic module layer. Appl Therm Eng 2023;223:119999.
[73] Tian R, Zhou S, Meng Y, Liu C, Ge Z. Material and device design of flexible perovskite solar cells for next-generation power supplies. Adv Mater 2024;36:2311473.
[74] R.K. Gupta, T.A. Nguyen, Smart and Flexible Energy Devices 2022, 1st ed., CRC Press. https://www.taylorfrancis.com/books/edit/10.1201/9781003186755/smart-flexible-energy-devices-ram-gupta-tuan-anh-nguyen.
[75] Jung HS, Han GS, Park NG, Ko MJ. Flexible perovskite solar cells. Joule 2019;3(8):1850–80.
[76] Goje AA, Ludin NA, Fahsyar PNA, et al. Review of flexible perovskite solar cells for indoor and outdoor applications. Mater Renewable Sustainable Energy 2024;13:155–79.
[77] Dai X, Deng Y, VanBrackle CH, Chen S, Rudd PN, Xiao X, et al. Scalable fabrication of efficient perovskite solar modules on flexible glass substrates. Adv Energy Mater 2020;10:1903108.
[78] Panidi J, Georgiadou DG, Schoetz T, Prodromakis T. Advances in organic and perovskite photovoltaics enabling a greener internet of things. Adv Funct Mater 2022;32:2200694.
[79] https://www.corning.com/media/worldwide/Innovation/documents/WillowGlass/Corning%20Willow%20Glass%20Fact%20Sheets_August2019.pdf (Accessed 12 October 2025).
[80] https://www.prnewswire.com/news-releases/energy-materials-corporation-sets-world-record-for-high-speed-roll-to-roll-printing-of-conductors-on-flexible-glass-for-perovskite-solar-panels-301208284.html (Accessed 12 October 2025).
[81] Corning Incorporated, 2021. Chemical vapor deposition of perovskite thin films. US Patent 11,094,881, United States. Available at: https://patents.google.com/patent/US11094881B2/en (Accessed 12 October 2025).
[82] X Li, Y. Zhang, J. Wang, 2018. Large area flexible perovskite solar cell. CN Patent 108011044B, China. Available at: https://patents.google.com/patent/CN108011044B/en (Accessed 12 October 2025).
[83] Palmstrom A, Eperon GE, Leijtens T, et al. Enabling flexible all-perovskite tandem solar cells. Joule 2019;3(9):2193–204.

[84] Wu P, Gangadharan DT, Saidaminov MI, Tan H. A roadmap for efficient and stable all-perovskite tandem solar cells from a chemistry perspective. ACS Cent Sci 2023;9(1):14–26.
[85] Li L, Wang Y, Wang X, et al. Flexible all-perovskite tandem solar cells approaching 25% efficiency with molecule-bridged hole-selective contact. Nat Energy 2022;7:708–17.
[86] Al-Sulaiman FA, Hamdullahpur F, Dincer I. Performance assessment of a novel system using parabolic trough solar collectors for combined cooling, heating, and power production. Renew Energy 2012;48:161–72.
[87] Herez A, Jaber H, El Hage H, Lemenand T, Chahine K, Ramadan M, et al. Parabolic trough photovoltaic thermoelectric hybrid system: simulation model, parametric analysis, and practical recommendations. Int J Thermofluids 2023;17:100309.
[88] Forristall R. Heat transfer analysis and modeling of a parabolic trough solar receiver implemented in engineering equation solver,. Nat Renew Energy Lab 2003.
[89] https://www.therminol.com/sites/therminol/files/documents/TF-8695_Therminol-66_Technical_Bulletin.pdf (Accessed 12 October 2025).
[90] K.E. Herold, R. Radermacher, A.K. Sanford, Absorption Chillers and Heat Pumps 2016, second ed. Taylor & Francis, London: CRC Press.
[91] Molés F, Navarro-Esbrí J, Peris B, Mota-Babiloni A, Barragán-Cervera A. Theoretical energy performance evaluation of different single stage vapour compression refrigeration configurations using R1234yf and R1234ze(E) as working fluids. Int J Refrig 2014;44:141–50.
[92] Mateu-Royo C, Navarro-Esbrí J, Mota-Babiloni A, Amat-Albuixech M, Molés F. Theoretical evaluation of different high-temperature heat pump configurations for low-grade waste heat recovery. Int J Refrig 2018;90:229–37.
[93] ANSI/ASHRAE Standard 15-2022 Safety Standard for Refrigeration Systems.
[94] Carmo M, Fritz DL, Mergel J, Stolten D. A comprehensive review on PEM water electrolysis. Int J Hydrogen Energy 2013;38(12):4901–34.
[95] García-Salaberri PA. 1D two-phase, non-isothermal modeling of a proton exchange membrane water electrolyzer: an optimization perspective. J Power Sources 2022;521:230915.
[96] Selamet OF, Acar MC, Mat MD, Kaplan Y. Effects of operating parameters on the performance of a high-pressure proton exchange membrane electrolyzer. Int J Energy Res 2013;37(5):457–67.
[97] Liso V, Savoia G, Araya SS, Cinti G, Kær SK. Modelling and experimental analysis of a polymer electrolyte membrane water electrolysis cell at different operating temperatures. Energies 2018;11:3273.
[98] A.S. Tijani, M.A. Ghani, A.A. Rahim, et al., Electrochemical characteristics of (PEM) electrolyzer under influence of charge transfer coefficient, International Journal of Hydrogen Energy 2019, 44(50):27177e89. https://www.sciencedirect.com/science/article/abs/pii/S0360319919332070?via%3Dihub.
[99] I. Dincer, A. Midilli, H. Kucuk, Progress in Exergy, Energy, and the Environment. Springer International Publishing 2014. https://link.springer.com/book/10.1007/978-3-319-04681-5.
[100] Hatsopoulous G, Keenan J. Principles of General Thermodynamics. New York: Wiley; 1965.
[101] Blanco-Marigorta AM, Marcos JD. Key issues on the exergetic analysis of H_2O/LiBr absorption cooling systems. Case Stud Therm Eng 2021;28:101568.
[102] J. Ahrendts, Die Exergie Chemisch Reaktionsfahiger Systeme, Düsseldorf. Germany: VDI-Verlag 1977.
[103] J. Szargut, Egzergia, Poradnik obliczania I stosowania, Widawnictwo Politechniki Shlaskej, Gliwice 2007.
[104] Ahmadi P, Dincer I, Rosen MA. Development and assessment of an integrated biomass-based multi-generation energy system. Energy 2013;56:155–66.
[105] I. Dincer, M.A Rosen, Chapter 2 - Exergy and Energy Analyses. Exergy (Second Edition), p.21-30, 2013b.
[106] Gaggioli RA. The dead state. Int J Thermodyn 2012;15:191–9.
[107] F.P. Incropera, D.P. DeWitt, Fundamentals of Heat and Mass Transfer, 5th ed.; John Wiley and Sons: New York, NY, USA, 2001.
[108] Zukauskas A. Heat transfer from tubes in crossflow. Adv Heat Tran 1987;8:87–159.
[109] Abedini-Ahangarkola H, Soleimani-Amiri S, Rudi SG. Modeling and numerical simulation of high efficiency perovskite solar cell with three active layers. Sol Energy 2022;236:724–32.
[110] P. Ahmadi, I. Dincer, M.A. Rosen, Energy and exergy analyses of hydrogen production via solar-boosted ocean thermal energy conversion and PEM electrolysis, International Journal of Hydrogen Energy 2013, 38(4):1795e805. https://www.sciencedirect.com/science/article/abs/pii/S0360319912024706?via%3Dihub.
[111] R. Garcia-Valverde, N. Espinosa, A. Urbina, Simple PEM water electrolyser model and experimental validation, International Journal of Hydrogen Energy 2012, 37(2):1927e38. https://www.sciencedirect.com/science/article/abs/pii/S0360319911021380?via%3Dihub.
[112] Gurau V, Barbir F, Liu HT. An analytical solution of a half-cell model for PEM fuel cells. J Electrochem Soc 2000;147(7):2468–77.
[113] F. Barbir, PEM electrolysis for production of hydrogen from renewable energy sources. Solar Energy 2005, 78(5):661e9. https://www.sciencedirect.com/science/article/abs/pii/S0038092X04002464?via%3Dihub.
[114] Görgün H. Dynamic modelling of a proton exchange membrane (PEM) electrolyzer. Int J Hydrogen Energy 2006;31:29e38.
[115] Yodwong B, Guilbert D, Phattanasak M, Kaewmanee W, Hinaje M, Vitale G. Faraday's efficiency modeling of a proton exchange membrane electrolyzer based on experimental data. Energies 2020;13:4792.
[116] Petela R. Exergy of undiluted thermal radiation. Sol Energy 2013;74:469–88.
[117] Lazzaretto A, Tsatsaronis G. Speco: a systematic and general methodology for calculating efficiencies and costs in thermal systems. Energy 2006;31(8–9):1257–89.
[118] Tsatsaronis G. Thermoeconomic analysis and optimization of energy systems. Prog Energy Combust Sci 1993;19:227–57.
[119] Sadiq M, Khan MS, Abid M, Alkahtani M, Xiaoming B. Exergo-economic analysis of a solar-driven multigeneration system for power, ammonia production, and cooling. Renew Energy 2025;248:123072.
[120] Mirmasoumi S, Saray RK, Asgari N. Exergy-based economic, environmental, and sustainability analysis of two different biogas-fueled trigeneration proposals for a wastewater treatment plant (WWTP). Energy 2025;326:136096.
[121] Habibollahzade A, Gholamian E, Ahmadi P, Behzadi A. Multi-criteria optimization of an integrated energy system with thermoelectric generator, parabolic trough solar collector and electrolysis for hydrogen production. Int J Hydrogen Energy 2018;43(31):14140–57.
[122] Deymi-Dashtebayaz M, Sulin A, Ryabova T, et al. Energy, exergoeconomic and environmental optimization of a cascade refrigeration system using different low GWP refrigerants. J Environ Chem Eng 2021;9(6):106473.
[123] https://ec.europa.eu/eurostat/statistics-explained/index.php?title=Electricity_price_statistics#Electricity_prices_for_non-household_consumers (Accessed 12 October 2025).
[124] https://ec.europa.eu/eurostat/statistics-explained/index.php?title=Natural_gas_price_statistics#Natural_gas_prices_for_non-household_consumers (Accessed 12 October 2025).
[125] https://greenenergy.mibgas.es/ (Accessed 12 October 2025).
[126] A. Bejan, G. Tsatsaronis, Thermal Design and Optimization, 1996, John Wiley & Sons.
[127] Khatoon S, Yadav SK, Chakravorty V, Singh J, et al. Perovskite solar cell's efficiency, stability and scalability: a review. Mater Sci Energy Technol 2023;6:437–59.
[128] Sharshir SW, El-Naggar AA, Ismail HA, Sami MM, et al. Degradation mechanisms and stability challenges in perovskite solar cells: a comprehensive review. Sol Energy 2025;299:113707.
[129] Ahn N, Choi M. Towards long-term stable perovskite solar cells: degradation mechanisms and stabilization techniques. Adv Sci 2024;11:2306110.
[130] Tiwari AK, Chatterjee K, Agrawal S, Singh GK. A comprehensive review of photovoltaic-thermal (PVT) technology: performance evaluation and contemporary development. Energy Rep 2023;10:2655–79.
[131] Chen K, Zuo J, Chang R. Compendium of degradation rates of global photovoltaic (PV) technology: insights from technology, climate and geography. Sol Energy Mater Sol Cells 2025;293:113839.
[132] Jamali A, Ahmadi P, Mohd Jaafar MN. Optimization of a novel carbon dioxide cogeneration system using artificial neural network and multi-objective genetic algorithm. Appl Therm Eng 2014;64:293–306.
[133] Anvari S, Taghavifar H, Saray RK, Khalilarya S, Jafarmadar S. Implementation of ANN on CCHP system to predict trigeneration performance with consideration of various operative factors. Energ Conver Manage 2015;101:503–14.
[134] Shannon CE. A mathematical theory of communication. Bell Syst Tech J 1948;27:379–423.
[135] Shakibi H, Nedaei N, Farajollahi AH, Chitsaz A. Exergoeconomic appraisement, sensitivity analysis, and multi-objective optimization of a solar-driven generation plant for yielding electricity and cooling load. Process Saf Environ Prot 2023;170:89–111.
[136] Liu Q, Zeng Z, Yang D, Liu W, et al. Multi-objective optimization and performance analysis of a CPV/T system based on NSGA-II and entropy weight TOPSIS method. Int J Heat Mass Transf 2026;255(2):127810.
[137] Zhu W, Han J, Ge Y, Yang J, Liang W. Multi-criteria optimization of a combined power and freshwater system using modified NSGA-II and AHP-entropy-topsis. Renew Energy 2024;227:120492.
[138] https://re.jrc.ec.europa.eu/pvg_tools/es/#TMY (Accessed 12 October 2025).